

1 Research Article

2

3

4 **Pathogenic neutrophilia drives acute respiratory distress syndrome**  
5 **in severe COVID-19 patients**

6

7 Running title: Pathogenic neutrophilia in severe COVID-19

8

9 **Devon J. Eddins<sup>1,2,3</sup>, Junkai Yang<sup>1,9</sup>, Astrid Kusters<sup>1,9</sup>, Vincent D. Giacalone<sup>2,4</sup>, Ximo**  
10 **Pechuan<sup>5</sup>, Joshua D. Chandler<sup>2,4</sup>, Jinyoung Eum<sup>1,6</sup>, Benjamin R. Babcock<sup>1</sup>, Brian S.**  
11 **Dobosh<sup>2,4</sup>, Mindy R. Hernández<sup>7</sup>, Fathma Abdulkhader<sup>1</sup>, Genoah L. Collins<sup>2,4</sup>, Richard P.**  
12 **Ramonell<sup>7</sup>, Christine Moussion<sup>5</sup>, Darya Y. Orlova<sup>5</sup>, Ignacio Sanz<sup>1,3,8</sup>, F. Eun-Hyung Lee<sup>1,3,7</sup>,**  
13 **Rabindra M. Tirouvanziam<sup>2,4</sup>, Eliver E.B. Ghosn<sup>1,2,3,6\*</sup>**

14

15 <sup>1</sup>Lowance Center for Human Immunology, Department of Medicine, Division of Immunology and  
16 Rheumatology, Emory University School of Medicine, Atlanta, GA 30322, USA

17

18 <sup>2</sup>Department of Pediatrics, Emory University School of Medicine, Atlanta, GA 30322, USA

19

20 <sup>3</sup>Emory Vaccine Center, Yerkes National Primate Research Center, Emory University School of  
21 Medicine, Atlanta, GA 30322, USA

22

23 <sup>4</sup>Center for CF & Airways Disease Research, Children's Healthcare of Atlanta, Atlanta, 30322  
24 GA, USA

25

26 <sup>5</sup>Genentech, Inc., South San Francisco, California 94080, USA

27

28 <sup>6</sup>Georgia Institute of Technology, Bioinformatics Graduate Program, Atlanta, GA 30332, USA

29

30 <sup>7</sup>Division of Pulmonary, Allergy, Critical Care & Sleep Medicine, Department of Medicine, Emory  
31 University School of Medicine, Atlanta, GA 30322, USA

32

33 <sup>8</sup>Emory Autoimmunity Center of Excellence, Department of Medicine, Division of Rheumatology,  
34 Emory University School of Medicine, Atlanta, GA 30322, USA

35

36 <sup>9</sup>These authors contributed equally: Junkai Yang and Astrid Kusters

37

38 **\*Corresponding Author Contact Info**

39

40 Eliver E.B. Ghosn (ORCID: 0000-0001-7258-906X): Lowance Center for Human Immunology,  
41 Health Sciences Research Building, 1760 Haygood Dr. NE, E240, Atlanta, GA 30322, USA; tel:  
42 +1-404-712-3211; email: [eliver.ghosn@emory.edu](mailto:eliver.ghosn@emory.edu)

33 **Abstract**

34

35 Severe acute respiratory syndrome coronavirus 2 (SARS-CoV-2) and the ensuing COVID-19  
36 pandemic have caused ~40 million cases and over 648,000 deaths in the United States alone.  
37 Troubling disparities in COVID-19-associated mortality emerged early, with nearly 70% of  
38 deaths confined to Black/African-American (AA) patients in some areas, yet targeted studies  
39 within this demographic are scant. Multi-omics single-cell analyses of immune profiles from  
40 airways and matching blood samples of Black/AA patients revealed low viral load, yet  
41 pronounced and persistent pulmonary neutrophilia with advanced features of cytokine release  
42 syndrome and acute respiratory distress syndrome (ARDS), including exacerbated production of  
43 IL-8, IL-1 $\beta$ , IL-6, and CCL3/4 along with elevated levels of neutrophil elastase and  
44 myeloperoxidase. Circulating S100A12<sup>+</sup>/IFITM2<sup>+</sup> mature neutrophils are recruited via the IL-  
45 8/CXCR2 axis, which emerges as a potential therapeutic target to reduce pathogenic  
46 neutrophilia and constrain ARDS in severe COVID-19.

## 47 Introduction

48

49 The coronavirus disease 2019 (COVID-19) pandemic, caused by SARS-CoV-2, is associated  
50 with high morbidity and mortality. To date, the pandemic has caused ~40 million cases and over  
51 648,000 deaths in the United States alone, where communities of color are disproportionately  
52 burdened with disease severity and mortality<sup>1, 2</sup>. A hallmark of COVID-19 pathogenesis is the  
53 vast array of clinical presentations and outcomes, ranging from asymptomatic or mild, self-  
54 limiting disease to acute respiratory distress syndrome (ARDS), multiorgan failure, and death.  
55 Indeed, such diversity in COVID-19 pathogenesis poses challenges to identify processes that  
56 dictate progression to severe disease. Early reports highlighted systemic hyperinflammatory  
57 responses that are linked to disease severity<sup>3</sup>. Cytokine release syndrome, also called a  
58 cytokine storm, has been observed in many patients and is suspected of causing the  
59 detrimental progression of COVID-19 and sustained immune dysregulation<sup>4</sup>.

60

61 Severe COVID-19 parallels the pathophysiology of sepsis<sup>5</sup>, where clinical presentation often  
62 includes granulocytosis, elevated proinflammatory cytokine production, aberrant myeloid  
63 activation, altered dendritic cell (DC) population dynamics, and lymphopenia<sup>6, 7</sup>. Early single-cell  
64 analyses of bronchoalveolar lavage fluid (BALF) samples implicated dysregulated monocyte  
65 and macrophage responses as central features in poor outcomes<sup>4, 8</sup>. As such, most early efforts  
66 have been focused on characterizing and constraining aberrant monocyte/macrophage  
67 responses. Concurrently, reports of neutrophilia in the peripheral blood arose, and the  
68 neutrophil to lymphocyte ratio emerged as an independent risk factor for disease progression<sup>9</sup>.  
69 Interestingly, a prior investigation of ARDS following sepsis identified sustained neutrophilia  
70 associated with worsened prognosis and death compared to patients who resolved neutrophilia  
71 and showed an increase in tissue-resident alveolar macrophages<sup>10</sup>, which may present another  
72 shared feature between COVID-19 and sepsis.

73

74 To date, there have been many studies of neutrophil responses in the blood of COVID-19  
75 patients<sup>11, 12, 13, 14, 15</sup>. However, an in-depth analysis of the neutrophil activity in the lungs is  
76 lacking. Expressly, the extent to which neutrophils contribute to cytokine release syndrome,  
77 tissue damage, and ultimately ARDS in severe COVID-19 cases is incompletely understood.  
78 Our systems immunology approach, combining high-dimensional (Hi-D, 30-parameter) flow  
79 cytometry and multi-omics single-cell sequencing analyses of immune profiles from the airways  
80 and matching blood samples of Black/African-American (AA) patients, revealed pronounced and  
81 sustained pulmonary neutrophilia as a hallmark of severe disease. Furthermore, mature  
82 pulmonary neutrophils produce very high levels of the neutrophil chemotactic factor IL-8 in  
83 addition to IL-1 $\beta$ , IL-6, and CCL3/4 along with copious amounts of neutrophil elastase (NE) and  
84 myeloperoxidase (MPO). Altogether, our findings highlight that transcriptionally active and highly  
85 inflammatory neutrophils are sustained in the airways of severe patients and that reducing  
86 pathogenic neutrophilia may constrain ARDS in severe COVID-19 disease.

87

## 88 **Results**

89

### 90 **Study Cohort**

91

92 To better understand immune dynamics in Black/AA patients with severe COVID-19, we  
93 analyzed airway and matching blood samples from a cohort of 35 individuals presenting to  
94 Emory University Hospitals (severe) or the Emory Acute Respiratory Clinic (mild-acute) in  
95 Atlanta, GA, USA (Fig. 1 and Extended Data Table 1), including 8 demographic-matched  
96 healthy adults as controls. Of the 27 individuals who were confirmed positive by PCR from  
97 nasopharyngeal swabs, 18 had an NIH severity score of "critical"  
98 (<https://www.covid19treatmentguidelines.nih.gov/overview/clinical-spectrum/>; referred to as  
99 severe herein) and were admitted to the intensive care unit (ICU) requiring mechanical ventilator  
100 support, and 9 were mild (mild-acute) outpatients. All severe patients in our cohort received  
101 corticosteroids (dexamethasone or equivalent). Approximately half received one or more doses  
102 of the antiviral medication remdesivir, with an average ICU stay of 26 days (see Extended Data  
103 Tables 1 and 2).

104

### 105 **Exacerbated neutrophilia in the airways and matching blood of severe COVID-19 patients**

106

107 We first characterized major immune lineages in the airways (endotracheal aspiration, ETA) and  
108 matching blood samples by Hi-D flow cytometry and observed a pronounced circulating  
109 neutrophilia and lymphopenia (notably T and NK cells), which is similarly reflected in the airways  
110 (Fig. 2a-e and Extended Data Fig. 1). This is in line with recent reports showing lymphopenia  
111 associated with significant alterations in the myeloid compartment<sup>15, 16</sup>. Strikingly, in most cases  
112 of severe disease,  $\geq 85\%$  of all pulmonary leukocytes were neutrophils (Fig. 2b). This contrasts  
113 with other studies that have reported much more heterogeneity in neutrophil frequency in  
114 patients' blood and lungs<sup>17, 18</sup>. In addition, circulating T cells and NK cells decline with increased  
115 disease severity (Fig. 2d), which has recently been reported as a feature of COVID-19  
116 pneumonia<sup>19</sup>. We also observed a notable decrease in pulmonary NK cells associated with  
117 disease severity (Fig. 2b). However, there were only subtle differences in the B-cell  
118 compartment (which were detected at very low levels in the airways) and myeloid-derived cells  
119 (MdCs) compartment compared to other reports<sup>8, 20, 21</sup>, highlighting the importance of  
120 neutrophilia and neutrophil-to-lymphocyte ratio in our cohort. Interestingly, the patient with the  
121 lowest neutrophil frequency in the airways corresponds to the youngest patient in the severe  
122 disease group (Fig. 2b). However, since we only had a single patient under 35 years old in our  
123 severe group, we cannot conclude any associations between neutrophilia and patient age.

124

125 Since we identified prominent neutrophilia in our cohort, we developed a Hi-D, 30-parameter  
126 flow cytometry panel to interrogate inflammatory neutrophil phenotype in addition to broad  
127 leukocyte characterization (see "CoV-Neutrophil" panel in Extended Data Table 3). Here, we  
128 used extracellular staining of neutrophil elastase (NE) and CD63 (LAMP3) to assess primary  
129 granule release<sup>22</sup>, coupled with intracellular staining for key effectors implicated in cytokine  
130 storm (IL-1 $\beta$ , IL-6, and IL-8). We observed that nearly all neutrophils recruited to the lung  
131 developed an inflammatory profile characterized by exacerbated levels of NE and elevated

132 production of IL-1 $\beta$  and IL-8 with a dramatic increase in primary granule release (Fig. 2c,e).  
133 Indeed, most neutrophils in the airways were positive for all 3 intracellular cytokines and  
134 express CD63 on the cell surface (Fig. 2c), suggesting that neutrophils are releasing cytokines  
135 upon degranulation. However, this phenotype is diminished in the circulation. A smaller  
136 proportion of blood neutrophils undergo granule release and express a cytokine signature  
137 limited mainly to IL-1 $\beta$  production and less IL-6 and IL-8 (Fig. 2e). Similarly, we find a subset of  
138 neutrophils in the lung that co-express the highest levels of surface CD10, CD184 (CXCR4) and  
139 NE (Fig. 2c). Interestingly, neutrophils in the lung express lower levels of Fc $\gamma$ RII (CD32) than  
140 those in the blood (Extended Data Fig. 5a). Together, these results demonstrate systemic  
141 neutrophilia in severe COVID-19 patients where neutrophils accumulating in the airways  
142 produce exacerbated levels of potentially damaging enzymes (e.g., NE) and inflammatory  
143 cytokines (IL-1 $\beta$ /6/8) while undergoing pronounced primary granule release.

144

### 145 **Neutrophil-secreted inflammatory molecules in the airways potentiate acute respiratory** 146 **distress syndrome in severe patients**

147

148 To better understand the inflammatory signaling milieu and relate the intracellular cytokine  
149 staining to protein secretion, we measured 21 total analytes in the airways and plasma using the  
150 Mesoscale UPLEX platform (Extended Data Table 4). We found that IL-8 is the most abundant  
151 chemokine in the airways of severe patients accompanied by high levels of IL-1 $\beta$  and IL-6. This  
152 is in line with our Hi-D flow cytometry data showing neutrophilia and pronounced intracellular  
153 staining signal for IL-8 and IL-1 $\beta$  (Fig. 3a-i). Strikingly, IL-8 levels were ~100-fold higher in the  
154 airways of severe versus mild patients and that of IL-1 $\beta$  and IL-6 levels in severe patients.  
155 These findings are in stark contrast to an early report<sup>23</sup> that showed no differences between  
156 circulating and pulmonary IL-6 and IL-8 secretion, reported in the <100 pg/mL range. However,  
157 more recent studies in both ETA<sup>24</sup> and BALF<sup>25</sup> samples have noted similar findings that  
158 corroborate our own. These data, therefore, implicate IL-8 signaling in the prominent  
159 neutrophilia observed in severe patients in our cohort.

160

161 We noticed only minor differences in circulating levels of many targets between healthy  
162 individuals and those affected by severe COVID-19 disease suggesting an uncoupling of local  
163 versus systemic inflammatory responses<sup>24</sup>, particularly for IL-8 and IL-1 $\beta$ , but also IL-6 to a  
164 lesser extent (Fig. 3a,d,g). Conversely, we observed a rise in circulating IL-1RA levels with  
165 increasing disease severity, similar to other reports<sup>26</sup>. However, we observed an opposite trend  
166 in the airways, where IL-1RA levels appear to be decreased in severe patients (Fig. 3j). This is  
167 in stark contrast to IL-1 $\beta$  levels, which were not markedly different in the circulation but  
168 significantly increased in the airways with disease severity (Fig. 3j). We also found increased  
169 CCL2 (MCP-1) in the airways of severe disease, and the same trend for M-CSF and TNF was  
170 observed, albeit at much lower concentrations (Fig. 3j). Interferon (IFN)- $\gamma$  was detected at the  
171 highest levels in the airways of severe patients with no obvious differentiation in plasma across  
172 all groups. IL-10 was also increased in the airways of severe patients with notable variation at  
173 low levels (Fig. 3j). In contrast to other studies<sup>27, 28</sup>, we did not observe appreciable differences  
174 in IL-18 or CXCL10 (IP-10) levels across patient groups (Extended Data Fig. 2). Additionally,

175 CXCL12 was not detected in the airways of patients, and there were no notable differences in  
176 plasma levels across patient groups (Extended Data Fig. 2).

177

178 We further measured the concentration of neutrophil-derived MPO and its enzymatic activity  
179 across patient groups. MPO is an important neutrophil effector molecule (originating from  
180 primary granules like NE) implicated in respiratory illnesses such as cystic fibrosis<sup>29</sup>, and can  
181 contribute to lung tissue damage during neutrophilic pneumonitis. MPO protein concentrations  
182 increased stepwise with disease severity in the plasma and respiratory supernatant (Fig. 3k).  
183 However, MPO activity was mostly detected in the airways, and rose with increasing disease  
184 severity (Fig. 3k).

185

### 186 **Recruited airway neutrophils are mature, transcriptionally active, and further differentiate** 187 **into a highly inflammatory state**

188

189 To gain insight into the cellular states and transcriptional regulation in patients with severe  
190 COVID-19 disease, we performed multi-omics scRNA-seq on cells from whole blood and ETA  
191 samples of severe patients and whole blood from demographic-matched healthy control (Fig. 1).  
192 We assessed immune features in data integrated from four or more patients from the same  
193 cohort (i.e., healthy vs. severe; see Methods). First, major lineages from blood (Fig. 4a) and  
194 ETA (Fig. 4g) were gated manually using the antibody-derived tag (ADT) data for surface  
195 protein expression. Next, we used the gene expression (GEX) data to generate clusters for  
196 each major lineage identified based on their surface markers, as per our previously described  
197 SuPERR-seq pipeline<sup>30</sup> (Extended Data Fig. 3). For example, neutrophils identified by CD66b  
198 and CD16 surface ADT in the blood (Fig. 4b) and ETA (Fig. 4h) were then selected and  
199 clustered independently by GEX data (Fig. 4c,i) for further analyses.

200

201 A prior study had reported an increase in immature neutrophils in the lung concomitant to  
202 increased circulating immature neutrophils from emergency hematopoiesis in severe COVID-19  
203 patients<sup>16</sup>. We, therefore, assessed the immature neutrophil phenotype in the blood (Fig 4a-e)  
204 and lung (Fig 4f-j) by scRNA-seq in our patient cohort. We readily identified a cluster of  
205 neutrophils expressing *CAMP*, *LTF*, *RETN*, *OLFM4*, *DEFA3*, *CD24*, and *MMP8* (Fig. 4e and  
206 Extended Data Fig. 4) in the blood of severe patients (cluster 3 in blood neutrophils) that also  
207 has high expression of calprotectin (S100A8/9) and other calgranulins (Fig 4d). This is  
208 consistent with immature neutrophil phenotypes described by others<sup>7, 15</sup> and was notably absent  
209 in neutrophils from healthy blood, confirming an emergency hematopoiesis/granulopoiesis in our  
210 patient cohort. However, in contrast to previous studies<sup>16</sup>, we did not observe any signature of  
211 immature neutrophils in the lungs of severe patients (Fig. 4j), suggesting that immature  
212 neutrophils either are not directly recruited to the lung, or quickly differentiate upon infiltration  
213 into the lung.

214

215 To determine which neutrophil subset in the blood can infiltrate the lung and further differentiate  
216 into a pathogenic state, we explored cell-cell communication (CellChat<sup>31</sup>) of clustered cells from  
217 blood (Fig. 4c) and lung (Fig. 4h) samples. We found significant communication through the  
218 CXCL pathway between the lung neutrophil, myeloid, and non-immune populations (i.e.,

219 epithelial/stromal cells) with *CXCR2*-expressing neutrophils from the blood (blood cluster 2; Fig.  
220 5a). The *CXCL8* (IL-8)/*CXCR2* pathway was identified as the primary recruitment axis for  
221 circulating *CXCR2*<sup>+</sup> neutrophils (Fig. 5b). These data are in line with our finding that IL-8 was  
222 increased in neutrophils by flow cytometry (Fig. 2) and secreted at very high levels in the  
223 airways (Fig. 3) and suggests that the *CXCL8*/*CXCR2* signaling axis is important for neutrophil  
224 recruitment to the lungs during COVID-19 pathogenesis. Virtually all lung neutrophils  
225 (particularly cluster 5), non-immune cells, and monocytes show the potential to recruit  
226 circulating neutrophils (Fig. 5a,d), indicating a robust and redundant mechanism of neutrophil  
227 recruitment to the airways via the *CXCL8*/*CXCR2* axis. Surprisingly, the immature neutrophils  
228 (blood cluster 3) lacked *CXCR2* (Fig. 5c), suggesting that immature neutrophils are unlikely to  
229 infiltrate the lung via IL-8. In contrast, a defined subset of mature neutrophils in blood  
230 expressing high levels of *CXCR2*, along with interferon-induced *IFITM2* and *S100A11/12*,  
231 identify blood cluster 2 as the putative neutrophil subset that can infiltrate the lung via IL-8 (Figs.  
232 4d and 5c-d). It is, therefore, probable that recent lung emigrants would still express detectable  
233 levels of *CXCR2*, as well as *IFITM2* and *S100A11/12* (Fig. 5c).

234  
235 After identifying the blood neutrophil cluster 2 as the putative source of lung-recruited  
236 neutrophils, we sought to identify their cell trajectory/differentiation once they enter the inflamed  
237 airway. Cell trajectory analyses (scVelo<sup>32</sup>) revealed two differentiation pathways (Trajectories 1  
238 and 2) for the recently infiltrated neutrophils (Fig. 5e). Indeed, cells expressing the highest levels  
239 of *CXCR2* and *S100A11/12* were at the beginning of the trajectory, further supporting these as  
240 the putative emigrant population from the blood (Fig. 5f). Notably, neutrophils recruited to the  
241 lung and differentiated along Trajectory 2 experience transcriptional reprogramming to acquire a  
242 heightened inflammatory phenotype (Fig. 5e,f). In contrast to the canonical neutrophil  
243 differentiation pathway, including a short half-life, the infiltrated neutrophils in severe COVID-19  
244 patients are transcriptionally active (Fig. 5e-g) in comparison to blood neutrophils (Extended  
245 Data Fig. 5b) and further differentiate into a hyperinflammatory state (Fig. 5f). This is consistent  
246 with more recent reports of neutrophil transmigration in other respiratory illnesses such as cystic  
247 fibrosis<sup>33</sup>, where neutrophils undergo lung/condition-specific adaptations upon recruitment from  
248 the circulation<sup>34</sup> instead of the canonical rapid and transient effector function proceeding cell  
249 death. Indeed, we observed increased expression of the interferon-stimulated gene (ISG) *IFI30*  
250 along with increased expression of *CCL3* (MIP-1 $\alpha$ ) and *CCL4* (MIP-1 $\beta$ ) (Fig. 5f), which in turn  
251 can promote the recruitment of inflammatory monocytes to the lung and/or proinflammatory  
252 macrophage phenotypes in the airways.

253  
254 Importantly, most neutrophils increase expression of *CXCL8* (IL-8) when recruited to the  
255 airways (Fig. 5d), perpetuating neutrophil recruitment to the lung. These findings further  
256 corroborate our Hi-D flow cytometry, gene expression, and secreted protein data analysis  
257 identifying IL-8 as the most abundant neutrophil-derived chemokine (and neutrophil chemotactic  
258 factor) in the airways of severe COVID-19 patients. Furthermore, most neutrophils increase the  
259 expression of *CXCR4* when recruited to the airways (Fig. 5f). Interestingly, we find that *CXCR4*  
260 expression, previously attributed to immature neutrophils<sup>16</sup>, is increased in mature lung-recruited  
261 neutrophils (Fig. 5f). This is consistent with *CXCR4* expression dynamics previously detected in  
262 non-COVID lung inflammation, including in cystic fibrosis<sup>35</sup> and malaria<sup>36</sup>. Taken together, the

263 progressive increase in *IFI30*, *CCL3/4*, along with abundant *de novo* *CXCL8* and *CXCR4* mRNA  
264 transcripts, reveal a transcriptionally active state in neutrophils that is poised to sustain a  
265 hyperinflammatory milieu in the lung of severe COVID-19 patients.

266

### 267 **Viral load in the respiratory tract does not correlate with disease severity**

268

269 We then investigated whether the recruited neutrophils or other cell types (i.e., myeloid,  
270 lymphoid, and non-immune cells) in the airways of severe patients were infected with SARS-  
271 CoV-2. By including the SARS-CoV-2 genome sequence into our human reference  
272 transcriptome in the multi-omics single-cell analysis, we were able to assess viral mRNA  
273 (vRNA) transcripts at a single-cell level (Fig. 7a). Notably, we did not detect vRNA in any cell  
274 types in the blood or airways of severe patients (Fig. 7b,c). Further, SARS-CoV-2-specific RT-  
275 qPCR revealed that viral load was decreased in the upper airways of severe patients admitted  
276 to the ICU compared to mild-acute patients (Fig. 7d,e). However, we did note a gene signature  
277 in neutrophils associated with response to IFN- $\gamma$  (Fig. 5g and Extended Data Fig. 5b), including  
278 a pronounced increase in *IFITM2* (Extended Data Fig. 5c), which has been shown to promote  
279 SARS-CoV-2 infection in human lung cells<sup>37</sup>.

280

281

### 282 **Pulmonary TNF and IL-1 $\beta$ promote neutrophil reprogramming in the lungs**

283

284 To ascertain which ligand-receptor pairs are potentially responsible for the transcriptional  
285 reprogramming of neutrophils in the lung, we first performed differential gene expression (DGE)  
286 analysis between blood neutrophil cluster 2 and lung neutrophils to identify genes that are  
287 upregulated in lung-recruited neutrophils (Fig. 6a). Next, we used the computational method  
288 NicheNet<sup>38</sup> to identify the potential (prioritized) ligands that could induce the upregulation of the  
289 genes identified by the DGE analysis, indicating their potential role in neutrophil reprogramming  
290 in the lung. *TNF*, *IL1B*, and *APOE* were the highest prioritized ligands with high ligand activity  
291 whose signaling axes have the regulatory potential to drive gene expression profiles observed in  
292 lung-recruited neutrophils (Fig. 6b). Importantly, NicheNet analysis revealed *TNF* as the ligand  
293 predicted to increase *BCL2A1* expression in pulmonary neutrophils, as well as *CCL4* (MIP-1 $\beta$ )  
294 and *CXCL16*. Furthermore, both *TNF* and *IL1B* are the ligands predicted to induce *NFKBIA* and  
295 *CXCL8* (IL-8), and *IL1B* shows the greatest potential to induce *CCL3* (MIP-1 $\alpha$ ) expression in  
296 recruited neutrophils. *APOE* is predicted to upregulate the expression of *FCER1G* in neutrophils  
297 in the lung. Notably, *TNF*, *IL1B*, and *HMGB1* are the ligands that have the widest range of  
298 regulatory potential, inducing neutrophil reprogramming by upregulating most genes that we  
299 identified as differentially expressed (Fig. 6a) in lung-recruited neutrophils (Fig 6b).

300

301 Pulmonary T cells represent the primary cell population expressing *TNF* in the airways, where  
302 MdCs have the highest *IL1B* and *APOE* transcripts (Fig. 6c,e). From the transcriptome data,  
303 ligand-receptor pair analyses further identified putative signaling mediators for the top 15  
304 prioritized ligands (Fig. 6d). *TNF* is predicted to signal through a receptor that has a *CALM1*  
305 association (Fig. 6d). Intriguingly, it has been previously reported that *CALM1* can bind other  
306 transmembrane proteins, including ACE-2<sup>39</sup>, and regulate their cell surface expression<sup>40</sup>. *IL1B* is  
307 predicted to signal through the canonical IL1B/IL1R2 pathway, and *APOE* through the  
308 APOE/SORL1 lipid pathway. *HMGB1* is predicted to signal through *LY96* (MD-2), which is  
309 commonly associated with TLR4 (Fig. 6d)<sup>41, 42, 43</sup>. Accordingly, *IL1R2* and *CALM1* transcripts are



310 abundant in neutrophils from blood cluster 2, and their expression are sustained upon  
311 recruitment to the airways (Fig. 6e).

312

313 Collectively, we show here that TNF- and IL-1 $\beta$ -mediated transcriptional reprogramming of lung  
314 infiltrating neutrophils leads to induction of proinflammatory *NFKBIA*, *CCL3* (MIP-1 $\alpha$ ), and *CCL4*  
315 (MIP-1 $\beta$ ) along with *TNFAIP3/6* and *CXCL8* (Figs. 5 and 6). Of note, neutrophil-derived *CCL3*  
316 and *CCL4* can attract inflammatory monocytes from the circulation to the airways. Interestingly,  
317 lung-infiltrating monocytes also produce elevated levels of *CXCL8*, potentiating the recruitment  
318 of circulating neutrophils via the *CXCL8/CXCR2* axis (Fig. 5a,d). Hence, both neutrophils and  
319 inflammatory monocytes in the airways exacerbate and potentiate pathogenic neutrophilia in the  
320 lungs of severe patients in a positive feedback loop.

## 321 Discussion

322  
323 Previous studies have reported increased neutrophilia in severe COVID-19, particularly in the  
324 circulation<sup>14, 44, 45, 46</sup>. In contrast, reports on exacerbated airway neutrophilia and the implication  
325 of lung neutrophils as the main cell type driving ARDS in severe patients have yielded  
326 inconclusive results<sup>7, 8, 17, 47</sup>. Here, we present the first comprehensive study of the lung immune  
327 response to SARS-CoV-2 in Black/AA individuals and unequivocally identify a robust and  
328 sustained airway neutrophilia associated with disease severity. The COVID-19 pandemic further  
329 highlighted some of the socio-economic and behavioral inequalities that may have contributed  
330 to troubling disparities in COVID-19-associated morbidity and mortality<sup>48</sup>, with almost 70% of  
331 deaths being Black/AA patients in some areas<sup>1, 2</sup>. Although the socio-economic and behavioral  
332 differences indeed contribute to health disparities among demographics, a systematic  
333 investigation to determine the immunological features that characterize disease severity within  
334 Black/AA patients is lacking. Our systems biology approach addresses this knowledge gap and  
335 reveals new therapeutic targets to inhibit neutrophil migration, retention, and/or survival in the  
336 lung as potential effective interventions for individuals with severe disease that have been  
337 disproportionately affected by COVID-19.

338  
339 Although previous studies on severe COVID-19 in humans have not been conclusive with  
340 regards to the role of airway neutrophilia in ARDS, studies in SARS-CoV-2-infected rhesus  
341 macaques and mice, where conditions and sample collection are more controlled, have  
342 identified exacerbated neutrophilia as a key immunological feature associated with disease  
343 severity<sup>49, 50, 51</sup>. Hence, taken together with previous studies on neutrophils<sup>8, 14, 17, 45, 46, 47</sup> along  
344 with animal models<sup>49, 50, 51</sup>, our current findings provide compelling evidence that targeting  
345 exacerbated airway neutrophilia may constrain ARDS and prevent further lung damage in most  
346 patients requiring mechanical ventilator support. Although our studies represent one of the few  
347 targeted investigations in Black/AA patients, we believe our results have broader implications  
348 and may apply to most patients suffering from neutrophilic ARDS<sup>11</sup>.

349  
350 The heightened numbers of neutrophils in the lung are likely to induce and sustain inflammatory  
351 signatures by an autocrine/paracrine feedback loop among neutrophils, and paracrine signaling  
352 to other cell types that can potentiate disease severity. Notably, NE is a potent serine protease  
353 that we show is released from degranulating neutrophils in the lungs (see Fig. 2), and has  
354 potential to stimulate production of TNF, IL-1 $\beta$ , and IL-8<sup>52, 53</sup>, and also abrogate protective  
355 effector functions of T cells and MdCs in the lung by cleaving cell surface receptors such as  
356 TLRs and Fc-receptors<sup>54, 55</sup>. Indeed, we demonstrate NE staining on the surface of T cells and  
357 MdCs in the lung (see Extended Data Fig. 5e) in addition to neutrophils, which may explain, in  
358 part, the reduction of Fc $\gamma$ RII (CD32) expression on pulmonary neutrophils (see Extended Data  
359 Fig. 5a). Of note, the reduction in CD32 expression may prevent IgG-mediated suppression of  
360 ISG induction<sup>14</sup> in pulmonary neutrophils. Indeed, we demonstrate a pronounced signature for  
361 the ISG *IFI30* (see Fig. 5f). Similarly, we show by intracellular staining that pulmonary  
362 neutrophils are producing exacerbated levels of IL-1 $\beta$  protein that is likely released upon  
363 degranulation along with IL-8 and IL-6 (see Figs. 2 and 3). In addition to neutrophils, the myeloid  
364 lineage is also abundant in the airways and as such they are poised to influence disease

365 progression. For example, we and others<sup>16</sup> have shown that infiltrating neutrophils sustain local  
366 production of calgranulins (S100A8/9/11/12), which can signal through and activate myeloid  
367 cells via TLRs and RAGE receptors, compounding the already hyperinflammatory lung milieu.  
368 Interestingly, the inflammatory monocytes that are likely recruited to the lungs via neutrophil-  
369 secreted CCL3/4 also show elevated levels of neutrophil chemotactic factor *CXCL8* (IL-8),  
370 which helps sustain recruitment of pathogenic neutrophils in a positive feedback loop.

371  
372 Other immune and non-immune cell populations in the lung may contribute to COVID-19  
373 pathogenesis in severe patients. Non-immune cells (e.g., stromal and epithelial cells) are known  
374 targets of SARS-CoV-2 in the lung<sup>56</sup>. Therefore, these cells are also posited to influence  
375 immune cell dynamics, especially at the outset of infection<sup>57</sup>. Indeed, our data indicate that non-  
376 immune cells play a role in granulocyte activation (Extended Data Fig. 5d) and therefore may  
377 initiate neutrophilia at the outset of infection<sup>58</sup>. Additionally, T cell-derived TNF and HMGB1,  
378 along with myeloid-derived IL-1 $\beta$ , have regulatory potential to induce inflammatory gene  
379 signatures observed in lung-recruited neutrophils. Strikingly, TNF is the ligand predicted to  
380 increase *BCL2A1* expression in pulmonary neutrophils, which is an anti-apoptotic factor known  
381 to regulate neutrophil survival<sup>59, 60</sup>. *TNF* signaling in recruited neutrophils also has the potential  
382 to drive *CCL4* (MIP-1 $\beta$ ) expression, along with *CXCL16*, which is another chemotactic factor  
383 that can recruit neutrophils and macrophages via the *CXCL16/CXCR6* pathway<sup>61, 62</sup>. In addition,  
384 myeloid-derived *APOE* is predicted to regulate the expression of *FCER1G* in lung-recruited  
385 neutrophils, which is associated with neutrophil activation during other viral respiratory  
386 infections<sup>63</sup>. Further studies should investigate other effector functions of myeloid and lymphoid  
387 subsets and how these cells interact with neutrophils to promote protection or pathology in the  
388 lungs of severe COVID-19 patients.

389  
390 Interestingly, *CXCR4* is upregulated in recruited neutrophils in severe patients (Figs. 4d,i and  
391 5f), which may promote neutrophil survival and retention during pneumonitis and/or further  
392 influence inflammatory neutrophil phenotype. Accordingly, *CXCR4* was shown to promote  
393 transcriptional reprogramming of neutrophils in pulmonary tissues<sup>64</sup>. Although we do not find  
394 detectable levels of the canonical *CXCR4* ligand (i.e., *CXCL12*) in the airways, we did observe  
395 transcripts for *HMGB1* (Fig. 6), which is an alternative ligand for *CXCR4*. Since the IL-8/*CXCR2*  
396 pathway is most notably increased and likely the primary neutrophil recruitment axis to the  
397 airways, we speculate that *CXCR4* signaling instead may promote neutrophil survival and  
398 retention at the site of inflammation, which has been previously reported<sup>65</sup>. Additionally, *CXCR4*  
399 signaling can stimulate de novo *CXCL8*/IL-8 production<sup>66, 67</sup>, and has been shown to promote  
400 neutrophil extracellular trap release during malaria disease progression<sup>68</sup>. Alternatively, *CXCR4*  
401 is also associated with neutrophil aging and senescence<sup>69, 70, 71</sup>. As such, elevated *CXCR4* may  
402 be associated with prolonged neutrophil survival in COVID-19 pathogenesis. In a prior study<sup>72</sup>,  
403 we noted a similar pattern of *CXCR4* expression on T cells from severe COVID-19 patients,  
404 where a progressive decrease of surface *CXCR4* is associated with recovery. In contrast,  
405 patients that succumbed to the disease, showed a time-dependent escalation in *CXCR4*<sup>+</sup>  
406 circulating T cells concomitant to increased *CXCR4*<sup>+</sup> T cells in the lungs<sup>72</sup>, implicating *CXCR4*  
407 on the dysregulated lung-homing inflammatory T cells in COVID-19. Further investigation into  
408 the potential role of *CXCR4* in cell survival, retention, or recruitment may unravel novel

409 therapeutic targets to modulate inflammation and treat severe COVID-19. Notably, therapeutic  
410 intervention with a CXCR4 antagonist during malaria-associated ARDS has shown significant  
411 benefit in animal models<sup>36</sup>.

412  
413 Modulating inflammation through corticosteroids (particularly dexamethasone) has shown  
414 clinical efficacy and is now the standard-of-care for patients progressing to severe COVID-19<sup>73</sup>.  
415 However, the pleiotropic effects of glucocorticoids and their propensity to cause neutrophilia are  
416 well documented in asthma and chronic obstructive pulmonary disease (COPD)<sup>74</sup>. Although a  
417 well-established mechanism of action for dexamethasone is via transcriptional repression of  
418 proinflammatory cytokines, we observed very high *CXCL8* and *IL1B* transcripts concomitant  
419 with elevated pulmonary IL-8 and IL-1 $\beta$  protein with prominent signatures by intracellular  
420 staining—particularly in pulmonary neutrophils. In contrast, IL-6 levels were lower than that of  
421 IL-8 and IL-1 $\beta$  in our patient cohort, and overly abundant neutrophils were not producing as  
422 much IL-6 comparatively, which may explain, in part, why anti-IL-6/IL-6R studies failed to meet  
423 primary endpoints<sup>75</sup>. Here, we provide evidence of an uncoupled cytokine profile in airway fluids  
424 versus plasma where the lung microenvironment exhibits features of cytokine-induced ARDS  
425 driven largely by a proinflammatory, neutrophilic feed-forward loop. Beyond COVID-19, it has  
426 been shown that resolution of neutrophilia in ARDS has substantial prognostic benefit<sup>10</sup>. Taken  
427 together, the *CXCL8* (IL-8)/CXCR2 signaling axis emerges as a key potential target for next-  
428 generation immunomodulatory therapy to reduce pathogenic neutrophilia and constrain severe  
429 disease in patients in addition to corticosteroids.

430  
431 We also contend that recognizing the lung pathology in severe COVID-19 to be a neutrophilic  
432 and hyperinflammatory disease is paramount to achieve better outcomes in next-generation  
433 therapies. Although the lung pathology in COVID-19 is initiated by a viral infection, severe  
434 patients in the ICU no longer show signs of uncontrolled viral replication. In fact, not only did we  
435 not detect viral transcripts by scRNA-seq within the cells in the airways, but we also noted  
436 decreased viral burden in severe patients in the ICU versus mild-acute patients seen in the  
437 outpatient clinic (Fig. 7). This is further supported by our previous study where we performed  
438 plaque assays on the respiratory secretions from severe patients and revealed significantly  
439 diminished, if any, viral plaques from the endotracheal aspirates<sup>76</sup>. This may explain, in part,  
440 why antiviral drugs such as remdesivir are not able to prevent death when administered to  
441 severe patients in ICU<sup>77</sup>.

442  
443 It is important to consider potentially confounding factors and limitations in our study. Though a  
444 major strength of our study is the uniformity of sample collection in a single disease state, our  
445 airway samples are limited to ETA, which contrasts with bronchoalveolar lavage fluid (BALF)  
446 used in other studies<sup>7, 17</sup>. The ETA procedure can sample material from the medial airways—  
447 i.e., an intermediate between the distal/lower airways (e.g., BALF) and the proximal/upper  
448 airways (e.g., sputum or oro-/naso-pharyngeal samples). Although the relative abundance of  
449 immune cells may vary across the upper and lower airways, previous studies observe a  
450 correlation between paired ETA and BALF samples. In addition, these studies show that ETA  
451 samples are not inherently neutrophilic<sup>78</sup>, though neutrophilia/granulocytosis may be a shared  
452 feature of non-COVID-19 and COVID-19 ARDS<sup>10, 79</sup>. In any event, our study is one of the only

453 known to date to employ integrated multi-omics single-cell investigation of immunity in  
454 exclusively Black/AA subjects, which are disproportionately burdened with severe disease and  
455 worse outcomes. Importantly, other studies of COVID-19 immune responses have noted similar  
456 features of disease severity<sup>7, 15, 16</sup>, which suggests that the findings in our target demographic  
457 will be broadly applicable to other groups. Finally, our study was limited in scope to 35 total  
458 subjects and single collection time points, limiting our abilities to interrogate correlations with  
459 clinical outcomes, warranting further longitudinal studies in larger patient cohorts.

460  
461 In conclusion, we present evidence that neutrophils are poised to be the leukocyte population  
462 most responsible for the dysregulated hyperinflammatory response that drives ARDS in severe  
463 COVID-19 patients. Neutrophil frequency and inflammatory profiles reveal that they are not only  
464 the most abundant leukocyte population in the medial airways, but also major producers of  
465 hallmark effector molecules associated with disease severity, including IL-8, IL-1 $\beta$ , and IL-6,  
466 along with potent proteases such as NE and MPO, which are inherently inflammatory and  
467 contribute to lung damage/pathology. Furthermore, we provide evidence for a neutrophil  
468 feedforward loop where IL-8, produced by virtually all pulmonary neutrophils (and some myeloid  
469 and stromal cells), is the primary chemokine recruiting circulating neutrophils and promoting  
470 neutrophilia in the inflamed airways.

471  
472 Collectively, our findings implicate neutrophilia in the immunopathophysiology of severe COVID-  
473 19 disease where perpetual, transcriptionally active, and highly inflammatory pulmonary  
474 neutrophils drive ARDS despite low viral burden. Thus, therapeutic intervention targeting  
475 neutrophil recruitment/retention and/or survival/reprogramming at the site of inflammation has  
476 the potential to constrain ARDS in severe patients, particularly those most vulnerable to  
477 succumb to COVID-19 disease.

478 **Methods**

479

480 **Ethics and biosafety.** A total of 35 individuals were recruited for this study (Extended Data  
481 Tables 1 and 2). The 18 severe COVID-19+ patients were recruited from the Intensive Care  
482 Units of Emory University, Emory St. Joseph's, Emory Decatur, and Emory Midtown Hospitals.  
483 We also recruited 9 mild COVID-19-infected outpatients in the Emory Acute Respiratory Clinic  
484 and 8 healthy adults from the Emory University Hospital. All studies were approved by the  
485 Emory Institutional Review Board (IRB) under protocol numbers IRB00058507, IRB00057983,  
486 and IRB00058271. Informed consent was obtained from the patients when they had decision-  
487 making ability or from a legally authorized representative (LAR) if the patient was unable to  
488 provide consent. Blood and sputum or endotracheal aspirate (ETA) were obtained. Control  
489 blood samples were obtained from healthy adults matched by age and race. Study inclusion  
490 criteria included a confirmed COVID-19 diagnosis by PCR amplification of SARS-CoV-2 viral  
491 RNA obtained from nasopharyngeal or oropharyngeal swabs, age of 18 years or greater, and  
492 willingness to provide informed consent. Individuals with a confirmed history of COVID-19  
493 diagnosis were excluded from the healthy donor group. All work with infectious virus and  
494 respiratory samples from COVID-19 patients was conducted inside a biosafety cabinet within  
495 the Emory Health and Safety Office (EHSO) and the United States Department of Agriculture  
496 (USDA)-approved BSL3 containment facility in the Health Sciences Research Building at Emory  
497 University following protocols approved by the Institutional Biosafety Committee (IBC) and  
498 Biosafety Officer (see ref<sup>76</sup>).

499

500 **Patient sample collection and processing.** Primary leukocytes from the airways of COVID-19  
501 patients requiring mechanical ventilator support were collected bedside via endotracheal  
502 aspiration (ETA) and whole blood collected by standard venipuncture. Plasma from whole blood  
503 was isolated via centrifugation at 400 x g for 10 min at 4°C. To remove platelets, the isolated  
504 plasma was centrifuged at 4,000 x g for 10 min at 4°C. Untouched circulating leukocytes were  
505 isolated using the EasySep™ RBC Depletion Reagent (StemCell Technologies). ETA (from  
506 severe patients) or non-induced sputum (from mild patients) was mixed 1:1 with a 50mM EDTA  
507 solution (final concentration 25 mM EDTA) in custom RPMI-1640 media deficient in biotin, L-  
508 glutamine, phenol red, riboflavin, and sodium bicarbonate (defRPMI-1640), with 3% newborn  
509 calf serum (NBCS) and mechanically dissociated using a syringe to liberate leukocytes from  
510 mucins and other respiratory secretions. Supernatants were collected for further analysis, and  
511 then cells underwent an additional mechanical dissociation step using 1-3 mL of a 10 mM EDTA  
512 in defRPMI-1640 + 3% NBCS and a P1000 pipettor. Cells were then washed with 10 mL  
513 defRPMI-1640 + 3% NBCS, passed through a 70 µm nylon strainer, and pelleted through a 2  
514 mL 100% NBCS layer prior to counting and downstream processing.

515

516 **High-dimensional (Hi-D) 30-parameter flow cytometry.** Cells (up to 10<sup>7</sup> total) were  
517 resuspended in defRPMI-1640 with 3% newborn calf serum and Benzonase™ (FACS buffer) in  
518 5 mL FACS tubes and pre-incubated with GolgiStop™ (BD Biosciences) for ~60 min at 4°C.  
519 Human TruStain FcX™ was then added, followed by a 10 min incubation at RT. The 24-color  
520 extracellular staining master mix (Extended Data Table 2) was prepared 2X in BD Horizon™  
521 Brilliant Stain Buffer to prevent staining artifacts from BD Horizon Brilliant dye interactions and

522 added 1:1 to cells, then incubated for 30 min at 4°C. Following staining (and total 1 h exposure  
523 to GolgiStop™), cells were washed with ~4 mL FACS buffer. Next, the cells were resuspended  
524 in 200 µL of BD Cytotfix/Cytoperm™ fixation/permeabilization solution and incubated at 4°C for  
525 30 min followed by a wash with ~4 mL BD Perm/Wash™ Buffer. The 4-color intracellular  
526 staining (Extended Data Table 3) was prepared in BD Perm/Wash™ Buffer, and cells were  
527 stained for 30 min at 4°C. Cells were washed with ~4 mL BD Perm/Wash™ Buffer, then  
528 resuspended for a final 20 min incubation in 4% PFA and transported out of the BSL3  
529 containment facility. Cells were washed in ~4 mL FACS buffer, then resuspended in 200-1000  
530 µL FACS buffer for acquisition using BD FACSDiva™ Software on the Emory Pediatric/Winship  
531 Flow Cytometry Core BD FACSymphony™ A5. To distinguish auto-fluorescent cells from cells  
532 expressing low levels of a particular surface marker, we established upper thresholds for auto-  
533 fluorescence by staining samples with fluorescence-minus-one (FMO) control stain sets in  
534 which a reagent for a channel of interest is omitted. Data were analyzed with FlowJo™ v10.8  
535 (FlowJo LLC).

536

537 **Cell-surface antibody-derived tag (ADT) staining, single-cell encapsulation, and library**  
538 **generation.** Leukocytes from whole blood and ETA samples were incubated with oligo-  
539 conjugated Ig-A/D/G/M for 10 min at 4°C followed by the addition of Human TruStain FcX™  
540 (BioLegend) and 10 min incubation at RT. Cells were then surface stained with oligo-conjugated  
541 monoclonal antibody panel (total 89 antibodies; Extended Data Table 5) for 30 min at 4°C,  
542 followed by two washes in def-RPMI-1640/0.04% BSA. Cells were resuspended at a  
543 concentration of 1200-1500 cells/µL in def-RPMI-1640/0.04% BSA and passed through a 20 or  
544 40 µm cell strainer before loading onto a Chromium Controller (10X Genomics, Pleasanton,  
545 CA). Cells were loaded to target encapsulation of 10,000 cells. Gene expression (GEX) and  
546 antibody-derived tag (ADT) libraries were generated using the Chromium Single Cell 5' Library  
547 & Gel Bead Kit v1.1 with feature barcoding following the manufacturer's instructions. GEX  
548 libraries were pooled and sequenced at a depth of approximately 540,000,000 reads per sample  
549 in a single S4 flow cell and ADT libraries at a depth of approximately 79,000,000 reads per  
550 sample in a single lane of an S4 flow cell on a NovaSeq™ 6000 (Illumina, San Diego, CA;  
551 Extended Data Table 6)

552

553 **Multi-omics single-cell RNA sequencing (scRNA-seq) analysis.** Single-cell 5' unique  
554 molecular identifier (UMI) counting and barcode de-multiplexing were performed using  
555 CellRanger Software (v.5.0.0). To detect SARS-CoV-2 viral RNA reads, we built a custom  
556 reference genome from human GRCh38 and SARS-CoV-2 references (severe acute respiratory  
557 syndrome coronavirus 2 isolate Wuhan-Hu-1, complete genome, GenBank MN908947.3).  
558 Splicing-aware aligner STAR<sup>80</sup> was implemented to align FASTQ inputs to the reference  
559 genome, and the resulting files are automatically filtered by CellRanger to include only cell  
560 barcodes representing real cells. This determination is based on the distribution of UMI counts.  
561 ADT reads were aligned to a feature reference file containing the antibody-specific barcode  
562 sequences. To recover neutrophils, we applied our SuPERR-seq pipeline as previously  
563 described<sup>30</sup>. Briefly, we recovered neutrophils from CellRanger unfiltered count matrices by  
564 plotting surface CD16 ADT and CD66b ADT using the "FeatureScatter" function in Seurat v4.0<sup>81</sup>  
565 (R version 4.0.2). The double-positive cell barcodes were then extracted and further evaluated

566 by GEX to confirm viable neutrophil identity. A threshold for mitochondrial content per barcode  
567 was determined for each sample independently and applied as a cutoff to remove dead or dying  
568 cells (Extended Data Table 7). Most samples show high cell viability with a minimal proportion of  
569 dead cells.

570  
571 The UMI counts of the GEX data were log-normalized by the "NormalizeData" function in Seurat  
572 before downstream analysis, following the optimal workflow we previously described for sample  
573 normalization and data integration<sup>82</sup>. Center log-ratio (CLR) transform in Seurat was performed  
574 on ADT UMIs when recovering neutrophils from the unfiltered matrices. For surface protein  
575 visualization to classify major lineages using our SuPERR-seq workflow<sup>30</sup>, ADT UMIs were  
576 normalized using the R package Denoised and Scaled by Background<sup>83</sup> (DSB) to remove  
577 ambient UMI counts (i.e., background) prior to manual sequential gating by surface expression  
578 (Extended Data Fig. 4) in SeqGeq v1.7 (FlowJo, LLC). DSB uses empty droplets to calculate  
579 background expression, which was manually selected according to the distribution of total ADT  
580 per cell in the raw count matrices (Extended Data Table 8). To minimize the influence from non-  
581 informative empty droplets, we removed cell barcodes with less than 100 total ADT UMIs before  
582 plotting the ADT distribution.

583  
584 Before integrating the multiple datasets, we first classified major lineages in individual samples  
585 based on a combination of gene transcript and surface protein markers (SuPERR-seq  
586 workflow<sup>30</sup>) as in Fig. 4 for samples where the ADT library was of sufficient quality to allow  
587 manual gating (Extended Data Fig. 4). Cell barcodes within each major lineage that co-  
588 expressed markers exclusive to other major lineages were considered cell doublets and  
589 removed (Extended Data Fig. 4). In addition, we removed cell barcodes with extremely high  
590 total ADT UMIs, which we considered to be aggregated cells. To efficiently integrate replicate  
591 samples, we concatenated major lineages derived from the same tissue in different donors. To  
592 minimize batch effects and optimize data integration, we followed the data normalization and  
593 merging strategies described previously<sup>82</sup>. Briefly, samples were first treated individually, and  
594 log-normalized count matrices were scaled/Z-transformed, and the "vst" method of the Seurat  
595 function "FindVariableFeatures" was utilized to select the top 1000 highly variable genes  
596 (HVGs) of each sample. HVGs shared between replicate samples were used to perform  
597 principal component analysis (PCA). To visualize the data, we performed UMAP reduction of  
598 the first 30 PCs, and cell clustering was generated using the Leiden community detection  
599 algorithm at a resolution of 0.8. UMAP visualizations for the integrated Blood and integrated  
600 ETA were generated using Seurat v4 data integration workflow.

601

602 **Receptor-ligand interaction analyses.** Clustered cells from lung and blood samples from each  
603 patient were investigated for evidence of intercellular communication using CellChat<sup>31</sup>.

604 Clustered cell populations from the lung samples were combined with the blood neutrophils to  
605 determine which lung cell populations could recruit circulating neutrophils. We utilized  
606 NicheNet<sup>38</sup> to determine which ligand-receptor pairs could be responsible for the different  
607 transcriptional states of the neutrophil populations in the lung and blood samples. We focused  
608 on certain neutrophil clusters as the receiver populations, considering the remaining neutrophils  
609 and other lung cell populations as the senders and thus potential interactors. The target set of



610 genes was determined using Seurat::FindMarkers(min.pct = 0.1), keeping only those genes with  
611 an adjusted p-value lower than 0.05 and average log2-fold change of more than 0.2. To address  
612 gene expression changes due to lung infiltration, we ran the algorithm using blood neutrophil  
613 cluster 2 as the most likely candidate for lung infiltration. The genes considered were those  
614 differentially expressed between blood cluster 2 and the lung neutrophils and genes  
615 differentially expressed between blood cluster 2 and those cells that progress along "Trajectory  
616 2" in the lung (see Fig.5).

617  
618 **Cell trajectory analyses.** The Python toolkit scVelo<sup>32</sup> inferred the trajectories using biological  
619 data of the ETA neutrophils. Input data for scVelo analysis was intron, exon, and spanning  
620 count matrices estimated using the dropEST tool<sup>84</sup>, then filtered with previously identified  
621 neutrophil cell barcodes in R studio. Intron, exon, and spanning matrices were compared to  
622 identify missing rows (genes) and were added to each matrix to equalize dimensions. The exon  
623 matrix contained the spliced matrix, and the sum of the intron and spanning matrices constituted  
624 the unspliced matrix. Spliced and unspliced matrices were imported with anndata library, and  
625 pandas library was used to import gene names and cell barcodes. Raw count matrices were  
626 added to anndata object layers as 'spliced' and 'unspliced.' Then, gene names and cell  
627 barcodes were attached to variables and observations of anndata object, respectively. Anndata  
628 object was transposed, followed by the regular scVelo analysis. The default parameters of  
629 plotting velocity streams include vkey='velocity', colorbar=True, alpha=0.3, sort\_order=True, and  
630 legend\_loc='on data'.

631  
632 **Pathway and process enrichment analyses.** Differential gene expression (DGE) analyses  
633 were performed in Seurat v4 and imported for gene annotation and further analysis using  
634 Metascape<sup>85</sup>. DGE between neutrophils versus the total ETA were used to generate Fig. 5g and  
635 non-immune cells versus total ETA were used for Extended Data Fig. 5d.

636  
637 **Mesoscale U-PLEX assays.** U-PLEX Biomarker Group 1 Human Multiplex Assays (Meso  
638 Scale Discovery) were used to evaluate levels of 21 analytes following the manufacturer's  
639 protocol (Extended Data Table 4) in plasma and UVC-inactivated respiratory supernatants (see  
640 ref<sup>76</sup>). Samples were diluted 1:5 for all assays except for IL-8, MCP-1, and IL-1RA, which were  
641 above the upper limit of detection for the assay and were diluted 1:200 to acquire measurement  
642 within the assay range. Final values were obtained by multiplying measurements by their  
643 respective dilution factor.

644  
645 **Myeloperoxidase (MPO) content and activity.** The abundance and activity of MPO were  
646 quantified as previously described<sup>29</sup>. MPO activity and protein concentration were measured  
647 sequentially following the immunocapture. On average, across six 96-well plate assays, lower  
648 limits of quantification were 4.0 ng/mL (activity) and 0.84 ng/mL (protein). Samples above the  
649 lower limit of detection but below the lower limit of quantification were imputed as half of the  
650 latter, and those detected above the highest standard of 50 ng/mL (i.e., above the upper limit of  
651 detection) at all dilutions were imputed as twice the standard concentration (Extended Data  
652 Table 4).

653

654 **SARS-CoV-2 quantitative reverse transcription PCR (RT-qPCR).** Viral (v)RNA was  
655 extracted from the respiratory secretions of COVID-19 patients using the *Quick-RNA*<sup>™</sup> Viral Kit  
656 (Zymo Research) following the manufacturer's protocol and complementary (c)DNA synthesized  
657 using the High-Capacity cDNA Reverse Transcription Kit (Applied Biosystems<sup>™</sup>) per the  
658 manufacturer's instructions, then diluted 1:5 in nuclease-free water. 10 µL diluted cDNA was  
659 used with the NEB Luna<sup>®</sup> Universal Probe qPCR Master Mix (New England BioLabs<sup>®</sup> Inc.)  
660 following the manufacturer's protocol and performed in 384-well plates using a QuantStudio<sup>™</sup> 5  
661 Real-Time PCR System (Applied Biosystems<sup>™</sup>). Primer/probe pairs were:  
662 AGAAGATTGGTTAGATGATGATAGT (forward), TTCCATCTCTAATTGAGGTTGAACC  
663 (reverse), and /56-FAM/TCCTCACTGCCGTCTTGTGACCA/3IABkFQ/ (probe), which were  
664 designed from sequences previously described<sup>86</sup> (Integrated DNA Technologies; IDT). To  
665 generate a standard curve for the quantification of SARS-CoV-2 genome copies a gBlock from  
666 IDT with the following sequence was used as a standard:  
667 AATTAAGAACACGTCACCGCAAGAAGAAGATTGGTTAGATGATGATAGTCAACAACTGTT  
668 GGTCAACAAGACGGCAGTGAGGACAATCAGACA ACTACTATTCAAACAATTGTTGAGGTTT  
669 AACCTCAATTAGAGATGGA ACTTACAGTTTCAGTGTTCAATTAA.

670  
671 **Statistical analyses.** Statistical analyses were performed using GraphPad Prism9. Data were  
672 analyzed for distribution (normal (Gaussian) vs. lognormal) independently using the D'Agostino  
673 and Pearson test for normality in the untransformed and Log10-transformed data. In cases  
674 where the sample size (*N*) was too small for D'Agostino and Pearson normality test, the  
675 Shapiro-Wilk test was used to assess distribution. When data passed both distribution tests, the  
676 likelihood of each distribution (normal vs. lognormal) was computed, and QQ-plots were  
677 generated. When Log10 transformed data had a higher likelihood of a normal distribution  
678 (passing normal distribution test) and/or failed lognormal distribution test, paired t-tests were  
679 performed to compare matching blood and respiratory supernatant samples within a single  
680 group. If the data had unequal variance (as determined by an F-test), a ratio paired t-test was  
681 performed. All instances where lognormal distribution was likely non-parametric Wilcoxon  
682 matched-pairs sign ranked tests were performed. For comparisons across the three patient  
683 groups (i.e., healthy, mild-acute, severe), ordinary one-way ANOVA (if equal variance) or  
684 Brown-Forsythe and Welch ANOVA (if unequal variance) tests were performed for data with a  
685 normal distribution. Alternatively, data with a lognormal distribution were analyzed with a  
686 Kruskal-Wallis test.

687  
688 **Data availability.** Single-cell sequencing datasets presented here are available through NCBI  
689 GEO, accession number XXX.

690 **Author Contributions**

691

692 **Devon J. Eddins:** Conceptualization, Methodology, Investigation, Formal Analysis, Data  
693 Curation, Writing–Original Draft, Writing–Review & Editing, Visualization. **Junkai Yang:**  
694 Methodology, Formal Analysis, Data Curation, Writing–Review & Editing, Visualization. **Astrid**  
695 **Kosters:** Methodology, Investigation, Data Curation, Writing–Review & Editing. **Vincent D.**  
696 **Giacalone:** Methodology, Formal Analysis, Investigation, Data Curation, Writing–Review &  
697 Editing. **Ximo Pechuan:** Methodology, Formal Analysis, Data Curation, Visualization, Writing–  
698 Review & Editing. **Joshua D. Chandler:** Methodology, Formal Analysis, Investigation, Data  
699 Curation, Writing–Review & Editing. **Jinyoung Eum:** Formal Analysis, Visualization. **Benjamin**  
700 **R. Babcock:** Investigation, Data curation. **Brian S. Dobosh:** Investigation, Data Curation,  
701 Formal Analysis. **Mindy R. Hernández:** Resources. **Fathma Abdulkhader:** Investigation.  
702 **Genoah L. Collins:** Investigation. **Richard P. Ramonell:** Resources, Data Curation, Writing–  
703 Review & Editing. **Christine Moussion:** Methodology, Formal Analysis. **Darya Y. Orlova:**  
704 Methodology, Data Curation. **Ignacio Sanz:** Resources. **F. Eun-Hyung Lee:** Methodology, Data  
705 Curation, Resources, Writing–Review & Editing. **Rabindra M. Tirouvanziam:** Methodology,  
706 Formal Analysis, Data Curation, Resources, Writing–Review & Editing. **Eliver E.B. Ghosn:**  
707 Conceptualization, Methodology, Formal Analysis, Resources, Data Curation, Writing–Original  
708 Draft, Visualization, Supervision, Project Administration, Funding Acquisition. All authors  
709 discussed the results and read and approved the final manuscript.

710

711 **Competing interests**

712

713 FEL is the founder of MicroB-plex, Inc., serves on the SAB of Be Bio Pharma, receives grants  
714 from BMGF and Genentech, and receives royalties from BLI, inc. All other authors have no  
715 competing interest to declare.

716

717 **Acknowledgments**

718

719 This study was funded by NIH/NIAID R01AI123126 (EEBG) and R01AI123126-05S1 (EEBG),  
720 the Program for Breakthrough Biomedical Research (EEBG), and the Lowance Center for  
721 Human Immunology (EEBG). DJE was partially supported by the Emory's Laney Graduate  
722 School Fellowship, and RPR was supported by the NIH T32-HL116271-07 Fellowship. The  
723 graphical abstract and Fig. 7d were generated in part using BioRender. We thank Keivan Zandi,  
724 Ann Chahroudi, Nils Schoof, Kira Moresco, and Stacy Heilman of the Department of Pediatrics  
725 (Emory University) along with the Emory Biosafety Officers Kalpana Rengarajan and Esmeralda  
726 Meyer for their assistance with setting up the BLS3 facility and kindly providing SARS-CoV-2  
727 viral stocks. We thank Nadia Roan (Gladstone Institutes/UCSF) and Sulggi Lee (UCSF) for  
728 helpful discussions. Flow cytometry data were collected at the Emory's Pediatrics/Winship Flow  
729 Cytometry Core (access supported in part by Children's Healthcare of Atlanta). We  
730 acknowledge the Genomic Cores at Yerkes Non-Human Primate Research Center at Emory  
731 University (NIH P51 OD011132; NIH S10 OD026799), Baylor College of Medicine, and the  
732 Parker H. Petit Institute for Bioengineering and Bioscience at the Georgia Institute of  
733 Technology for the single-cell library sequences. We are grateful for the efforts of Sang N. Le,  
734 John Varghese, Anum Jalal, Saeyun Lee, and Rahul Patel, who also contributed to patient  
735 recruitment. We also thank the nurses, staff, and providers in the 71 ICU in Emory University  
736 Hospital Midtown, the medical ICU in Emory Decatur Hospital, the 5G/6G ICU in Emory  
737 University Hospital, and the ICU in Emory Saint Joseph's Hospital for their dedication and  
738 commitment during the COVID-19 pandemic. We thank all healthy individuals, patients, and  
739 their families for their participation in this study, without whom our work would not have been  
740 possible.

741 **References**

- 742 1. Van Dyke, M.E. *et al.* Racial and ethnic disparities in COVID-19 incidence by age, sex,  
743 and period among persons aged < 25 years—16 US jurisdictions, January 1–December  
744 31, 2020. *Morbidity and Mortality Weekly Report* **70**, 382 (2021).  
745
- 746 2. Romano, S.D. *et al.* Trends in Racial and Ethnic Disparities in COVID-19  
747 Hospitalizations, by Region - United States, March-December 2020. *MMWR Morb Mortal*  
748 *Wkly Rep* **70**, 560-565 (2021).  
749
- 750 3. Lucas, C. *et al.* Longitudinal analyses reveal immunological misfiring in severe COVID-  
751 19. *Nature* **584**, 463-469 (2020).  
752
- 753 4. Merad, M. & Martin, J.C. Pathological inflammation in patients with COVID-19: a key role  
754 for monocytes and macrophages. *Nature Reviews Immunology* **20**, 355-362 (2020).  
755
- 756 5. Olwal, C.O. *et al.* Parallels in Sepsis and COVID-19 Conditions: Implications for  
757 Managing Severe COVID-19 Patients. *Frontiers in immunology* **12**, 91 (2021).  
758
- 759 6. Carvalho, T., Krammer, F. & Iwasaki, A. The first 12 months of COVID-19: a timeline of  
760 immunological insights. *Nat Rev Immunol* **21**, 245-256 (2021).  
761
- 762 7. Bost, P. *et al.* Deciphering the state of immune silence in fatal COVID-19 patients. *Nat*  
763 *Commun* **12**, 1428 (2021).  
764
- 765 8. Liao, M. *et al.* Single-cell landscape of bronchoalveolar immune cells in patients with  
766 COVID-19. *Nat Med* **26**, 842-844 (2020).  
767
- 768 9. Liang, W. *et al.* Development and Validation of a Clinical Risk Score to Predict the  
769 Occurrence of Critical Illness in Hospitalized Patients With COVID-19. *JAMA Intern Med*  
770 **180**, 1081-1089 (2020).  
771
- 772 10. Steinberg, K.P. *et al.* Evolution of bronchoalveolar cell populations in the adult  
773 respiratory distress syndrome. *Am J Respir Crit Care Med* **150**, 113-122 (1994).  
774
- 775 11. Barnes, B.J. *et al.* Targeting potential drivers of COVID-19: Neutrophil extracellular  
776 traps. *J Exp Med* **217** (2020).  
777
- 778 12. Kong, M., Zhang, H., Cao, X., Mao, X. & Lu, Z. Higher level of neutrophil-to-lymphocyte  
779 is associated with severe COVID-19. *Epidemiology & Infection* **148** (2020).  
780
- 781 13. Liu, Y. *et al.* Neutrophil-to-lymphocyte ratio as an independent risk factor for mortality in  
782 hospitalized patients with COVID-19. *Journal of Infection* (2020).  
783
- 784 14. Combes, A.J. *et al.* Global absence and targeting of protective immune states in severe  
785 COVID-19. *Nature* **591**, 124-130 (2021).  
786
- 787 15. Schulte-Schrepping, J. *et al.* Severe COVID-19 is marked by a dysregulated myeloid cell  
788 compartment. *Cell* **182**, 1419-1440 (2020).  
789
- 790 16. Silvin, A. *et al.* Elevated Calprotectin and Abnormal Myeloid Cell Subsets Discriminate  
791 Severe from Mild COVID-19. *Cell* **182**, 1401-1418 e1418 (2020).

- 792  
793 17. Grant, R.A. *et al.* Circuits between infected macrophages and T cells in SARS-CoV-2  
794 pneumonia. *Nature* **590**, 635-641 (2021).  
795  
796 18. Wilk, A.J. *et al.* A single-cell atlas of the peripheral immune response in patients with  
797 severe COVID-19. *Nat Med* **26**, 1070-1076 (2020).  
798  
799 19. Kreutmair, S. *et al.* Distinct immunological signatures discriminate severe COVID-19  
800 from non-SARS-CoV-2-driven critical pneumonia. *Immunity* **54**, 1578-1593 e1575  
801 (2021).  
802  
803 20. Ren, X. *et al.* COVID-19 immune features revealed by a large-scale single-cell  
804 transcriptome atlas. *Cell* **184**, 1895-1913 e1819 (2021).  
805  
806 21. Xu, G. *et al.* The differential immune responses to COVID-19 in peripheral and lung  
807 revealed by single-cell RNA sequencing. *Cell Discov* **6**, 73 (2020).  
808  
809 22. Forrest, O.A. *et al.* Frontline Science: Pathological conditioning of human neutrophils  
810 recruited to the airway milieu in cystic fibrosis. *J Leukoc Biol* **104**, 665-675 (2018).  
811  
812 23. Szabo, P.A. *et al.* Longitudinal profiling of respiratory and systemic immune responses  
813 reveals myeloid cell-driven lung inflammation in severe COVID-19. *Immunity* **54**, 797-  
814 814 (2021).  
815  
816 24. Jouan, Y., Baranek, T., Si-Tahar, M., Paget, C. & Guillon, A. Lung compartmentalization  
817 of inflammatory biomarkers in COVID-19-related ARDS. *Critical Care* **25**, 1-3 (2021).  
818  
819 25. Zaid, Y. *et al.* Chemokines and Eicosanoids Fuel the Hyperinflammation Within the  
820 Lungs of Patients with Severe COVID-19. *Journal of Allergy and Clinical Immunology*  
821 (2021).  
822  
823 26. Jouan, Y. *et al.* Phenotypical and functional alteration of unconventional T cells in severe  
824 COVID-19 patients. *J Exp Med* **217** (2020).  
825  
826 27. Satiş, H. *et al.* Prognostic value of interleukin-18 and its association with other  
827 inflammatory markers and disease severity in COVID-19. *Cytokine* **137**, 155302 (2021).  
828  
829 28. Yang, Y. *et al.* Plasma IP-10 and MCP-3 levels are highly associated with disease  
830 severity and predict the progression of COVID-19. *Journal of Allergy and Clinical*  
831 *Immunology* **146**, 119-127 (2020).  
832  
833 29. Chandler, J.D. *et al.* Myeloperoxidase oxidation of methionine associates with early  
834 cystic fibrosis lung disease. *Eur Respir J* **52** (2018).  
835  
836 30. Xu, C. *et al.* Comprehensive multi-omics single-cell data integration reveals greater  
837 heterogeneity in the human immune system. *bioRxiv*, 2021.2007.2025.453651 (2021).  
838  
839 31. Jin, S. *et al.* Inference and analysis of cell-cell communication using CellChat. *Nature*  
840 *communications* **12**, 1-20 (2021).  
841

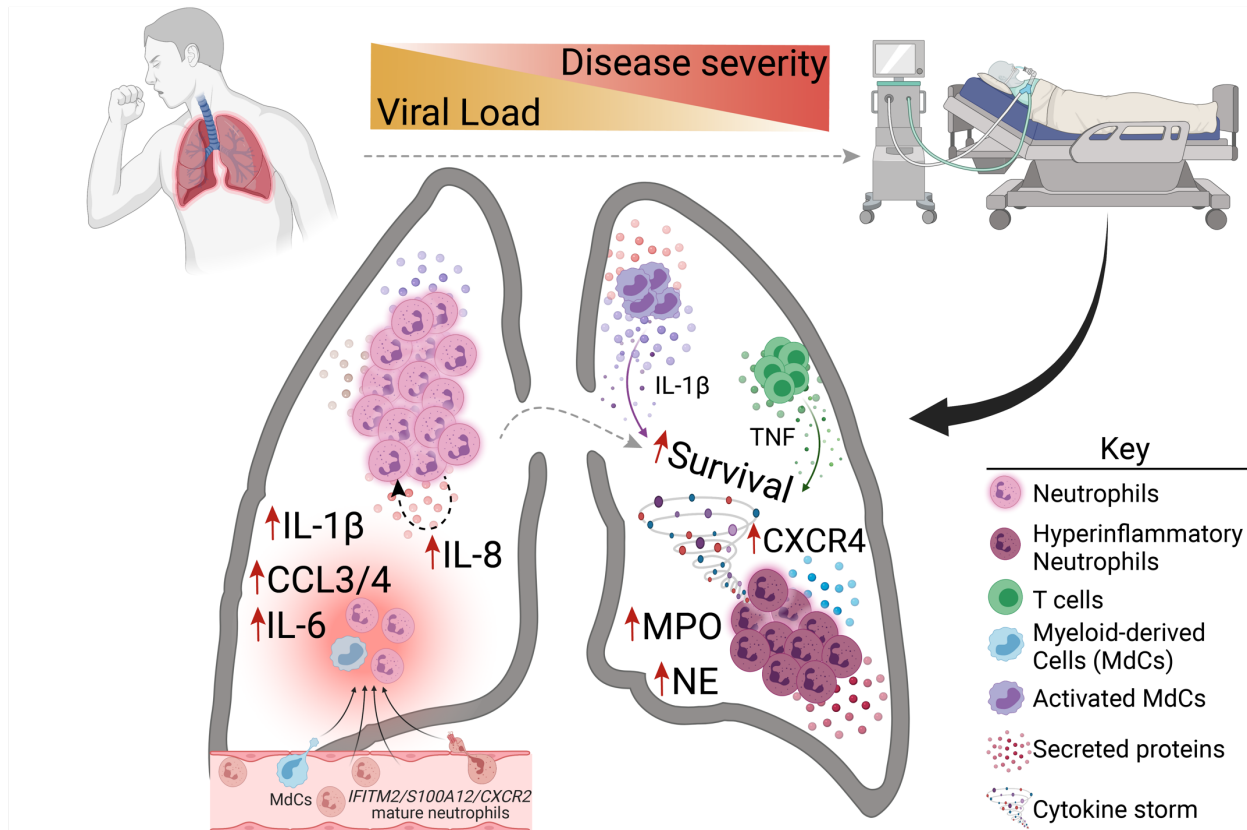
- 842 32. Bergen, V., Lange, M., Peidli, S., Wolf, F.A. & Theis, F.J. Generalizing RNA velocity to  
843 transient cell states through dynamical modeling. *Nat Biotechnol* **38**, 1408-1414 (2020).  
844
- 845 33. Margaroli, C. *et al.* Transcriptional firing represses bactericidal activity in cystic fibrosis  
846 airway neutrophils. *Cell Rep Med* **2**, 100239 (2021).  
847
- 848 34. Giacalone, V.D., Margaroli, C., Mall, M.A. & Tirouvanziam, R. Neutrophil Adaptations  
849 upon Recruitment to the Lung: New Concepts and Implications for Homeostasis and  
850 Disease. *International Journal of Molecular Sciences* **21**, 851 (2020).  
851
- 852 35. Makam, M. *et al.* Activation of critical, host-induced, metabolic and stress pathways  
853 marks neutrophil entry into cystic fibrosis lungs. *Proc Natl Acad Sci U S A* **106**, 5779-  
854 5783 (2009).  
855
- 856 36. Sercundes, M.K. *et al.* Targeting Neutrophils to Prevent Malaria-Associated Acute Lung  
857 Injury/Acute Respiratory Distress Syndrome in Mice. *PLoS Pathog* **12**, e1006054 (2016).  
858
- 859 37. Prelli Bozzo, C. *et al.* IFITM proteins promote SARS-CoV-2 infection and are targets for  
860 virus inhibition in vitro. *Nature Communications* **12**, 1-13 (2021).  
861
- 862 38. Browaeys, R., Saelens, W. & Saeys, Y. NicheNet: modeling intercellular communication  
863 by linking ligands to target genes. *Nat Methods* **17**, 159-162 (2020).  
864
- 865 39. Chattopadhyay, S. *et al.* Calmodulin binds to the cytoplasmic domain of angiotensin-  
866 converting enzyme and regulates its phosphorylation and cleavage secretion. *J Biol*  
867 *Chem* **280**, 33847-33855 (2005).  
868
- 869 40. Lambert, D.W., Clarke, N.E., Hooper, N.M. & Turner, A.J. Calmodulin interacts with  
870 angiotensin-converting enzyme-2 (ACE2) and inhibits shedding of its ectodomain. *FEBS*  
871 *letters* **582**, 385-390 (2008).  
872
- 873 41. Shimazu, R. *et al.* MD-2, a molecule that confers lipopolysaccharide responsiveness on  
874 Toll-like receptor 4. *J Exp Med* **189**, 1777-1782 (1999).  
875
- 876 42. Visintin, A., Mazzone, A., Spitzer, J.A. & Segal, D.M. Secreted MD-2 is a large polymeric  
877 protein that efficiently confers lipopolysaccharide sensitivity to Toll-like receptor 4. *Proc*  
878 *Natl Acad Sci U S A* **98**, 12156-12161 (2001).  
879
- 880 43. Yang, H. *et al.* A critical cysteine is required for HMGB1 binding to Toll-like receptor 4  
881 and activation of macrophage cytokine release. *Proc Natl Acad Sci U S A* **107**, 11942-  
882 11947 (2010).  
883
- 884 44. Bohn, M.K. *et al.* Pathophysiology of COVID-19: Mechanisms Underlying Disease  
885 Severity and Progression. *Physiology (Bethesda)* **35**, 288-301 (2020).  
886
- 887 45. Meizlish, M.L. *et al.* A neutrophil activation signature predicts critical illness and mortality  
888 in COVID-19. *Blood Adv* **5**, 1164-1177 (2021).  
889
- 890 46. Metzemaekers, M. *et al.* Kinetics of peripheral blood neutrophils in severe coronavirus  
891 disease 2019. *Clin Transl Immunology* **10**, e1271 (2021).  
892

- 893 47. Wauters, E. *et al.* Discriminating mild from critical COVID-19 by innate and adaptive  
894 immune single-cell profiling of bronchoalveolar lavages. *Cell Res* **31**, 272-290 (2021).  
895
- 896 48. Abedi, V. *et al.* Racial, economic, and health inequality and COVID-19 infection in the  
897 United States. *Journal of racial and ethnic health disparities* **8**, 732-742 (2021).  
898
- 899 49. Guo, Q. *et al.* Induction of alarmin S100A8/A9 mediates activation of aberrant  
900 neutrophils in the pathogenesis of COVID-19. *Cell Host Microbe* **29**, 222-235 e224  
901 (2021).  
902
- 903 50. Hoang, T.N. *et al.* Baricitinib treatment resolves lower-airway macrophage inflammation  
904 and neutrophil recruitment in SARS-CoV-2-infected rhesus macaques. *Cell* **184**, 460-  
905 475 e421 (2021).  
906
- 907 51. Vanderheiden, A. *et al.* CCR2-dependent monocyte-derived cells restrict SARS-CoV-2  
908 infection. *bioRxiv* (2021).  
909
- 910 52. Krotova, K., Khodayari, N., Oshins, R., Aslanidi, G. & Brantly, M.L. Neutrophil elastase  
911 promotes macrophage cell adhesion and cytokine production through the integrin-Src  
912 kinases pathway. *Sci Rep* **10**, 15874 (2020).  
913
- 914 53. Towstyka, N.Y. *et al.* Modulation of  $\gamma\delta$  T-cell activation by neutrophil elastase.  
915 *Immunology* **153**, 225-237 (2018).  
916
- 917 54. Domon, H. *et al.* Neutrophil Elastase Subverts the Immune Response by Cleaving Toll-  
918 Like Receptors and Cytokines in Pneumococcal Pneumonia. *Front Immunol* **9**, 732  
919 (2018).  
920
- 921 55. Kim, E. *et al.* Inhibition of elastase enhances the adjuvanticity of alum and promotes  
922 anti-SARS-CoV-2 systemic and mucosal immunity. *Proc Natl Acad Sci U S A* **118**  
923 (2021).  
924
- 925 56. Delorey, T.M. *et al.* COVID-19 tissue atlases reveal SARS-CoV-2 pathology and cellular  
926 targets. *Nature* **595**, 107-113 (2021).  
927
- 928 57. Chua, R.L. *et al.* COVID-19 severity correlates with airway epithelium-immune cell  
929 interactions identified by single-cell analysis. *Nat Biotechnol* **38**, 970-979 (2020).  
930
- 931 58. Qi, F. *et al.* ScRNA-seq revealed the kinetic of nasopharyngeal immune responses in  
932 asymptomatic COVID-19 carriers. *Cell Discov* **7**, 56 (2021).  
933
- 934 59. Jenal, M. *et al.* The anti-apoptotic gene BCL2A1 is a novel transcriptional target of PU.1.  
935 *Leukemia* **24**, 1073-1076 (2010).  
936
- 937 60. Vier, J., Groth, M., Sochalska, M. & Kirschnek, S. The anti-apoptotic Bcl-2 family protein  
938 A1/Bfl-1 regulates neutrophil survival and homeostasis and is controlled via PI3K and  
939 JAK/STAT signaling. *Cell Death Dis* **7**, e2103 (2016).  
940
- 941 61. Woehrl, B. *et al.* CXCL16 contributes to neutrophil recruitment to cerebrospinal fluid in  
942 pneumococcal meningitis. *J Infect Dis* **202**, 1389-1396 (2010).  
943



- 944 62. Zhang, L. *et al.* Chemokine CXCL16 regulates neutrophil and macrophage infiltration  
945 into injured muscle, promoting muscle regeneration. *Am J Pathol* **175**, 2518-2527  
946 (2009).  
947
- 948 63. Besteman, S.B. *et al.* Transcriptome of airway neutrophils reveals an interferon  
949 response in life-threatening respiratory syncytial virus infection. *Clinical Immunology*  
950 **220**, 108593 (2020).  
951
- 952 64. Ballesteros, I. *et al.* Co-option of Neutrophil Fates by Tissue Environments. *Cell* **183**,  
953 1282-1297 e1218 (2020).  
954
- 955 65. Yamada, M. *et al.* The increase in surface CXCR4 expression on lung extravascular  
956 neutrophils and its effects on neutrophils during endotoxin-induced lung injury. *Cell Mol*  
957 *Immunol* **8**, 305-314 (2011).  
958
- 959 66. Bernhagen, J. *et al.* MIF is a noncognate ligand of CXC chemokine receptors in  
960 inflammatory and atherogenic cell recruitment. *Nature medicine* **13**, 587-596 (2007).  
961
- 962 67. Pawig, L., Klasen, C., Weber, C., Bernhagen, J. & Noels, H. Diversity and Inter-  
963 Connections in the CXCR4 Chemokine Receptor/Ligand Family: Molecular  
964 Perspectives. *Front Immunol* **6**, 429 (2015).  
965
- 966 68. Rodrigues, D.A.S. *et al.* CXCR4 and MIF are required for neutrophil extracellular trap  
967 release triggered by Plasmodium-infected erythrocytes. *PLoS pathogens* **16**, e1008230  
968 (2020).  
969
- 970 69. Adrover, J.M. *et al.* A neutrophil timer coordinates immune defense and vascular  
971 protection. *Immunity* **50**, 390-402 (2019).  
972
- 973 70. Casanova-Acebes, M. *et al.* Rhythmic modulation of the hematopoietic niche through  
974 neutrophil clearance. *Cell* **153**, 1025-1035 (2013).  
975
- 976 71. Ng, L.G., Ostuni, R. & Hidalgo, A. Heterogeneity of neutrophils. *Nature Reviews*  
977 *Immunology* **19**, 255-265 (2019).  
978
- 979 72. Neidleman, J. *et al.* Distinctive features of SARS-CoV-2-specific T cells predict recovery  
980 from severe COVID-19. *medRxiv* (2021).  
981
- 982 73. Group, R.C. Dexamethasone in hospitalized patients with Covid-19. *New England*  
983 *Journal of Medicine* **384**, 693-704 (2021).  
984
- 985 74. Ronchetti, S., Ricci, E., Migliorati, G., Gentili, M. & Riccardi, C. How glucocorticoids  
986 affect the neutrophil life. *International journal of molecular sciences* **19**, 4090 (2018).  
987
- 988 75. Mullard, A. Anti-IL-6Rs falter in COVID-19. *Nat Rev Drug Discov* **19**, 577 (2020).  
989
- 990 76. Eddins, D.J. *et al.* Inactivation of SARS Coronavirus 2 and COVID-19 patient samples  
991 for contemporary immunology studies. *bioRxiv* (2021).  
992
- 993 77. Beigel, J.H. *et al.* Remdesivir for the Treatment of Covid-19 - Final Report. *N Engl J Med*  
994 **383**, 1813-1826 (2020).

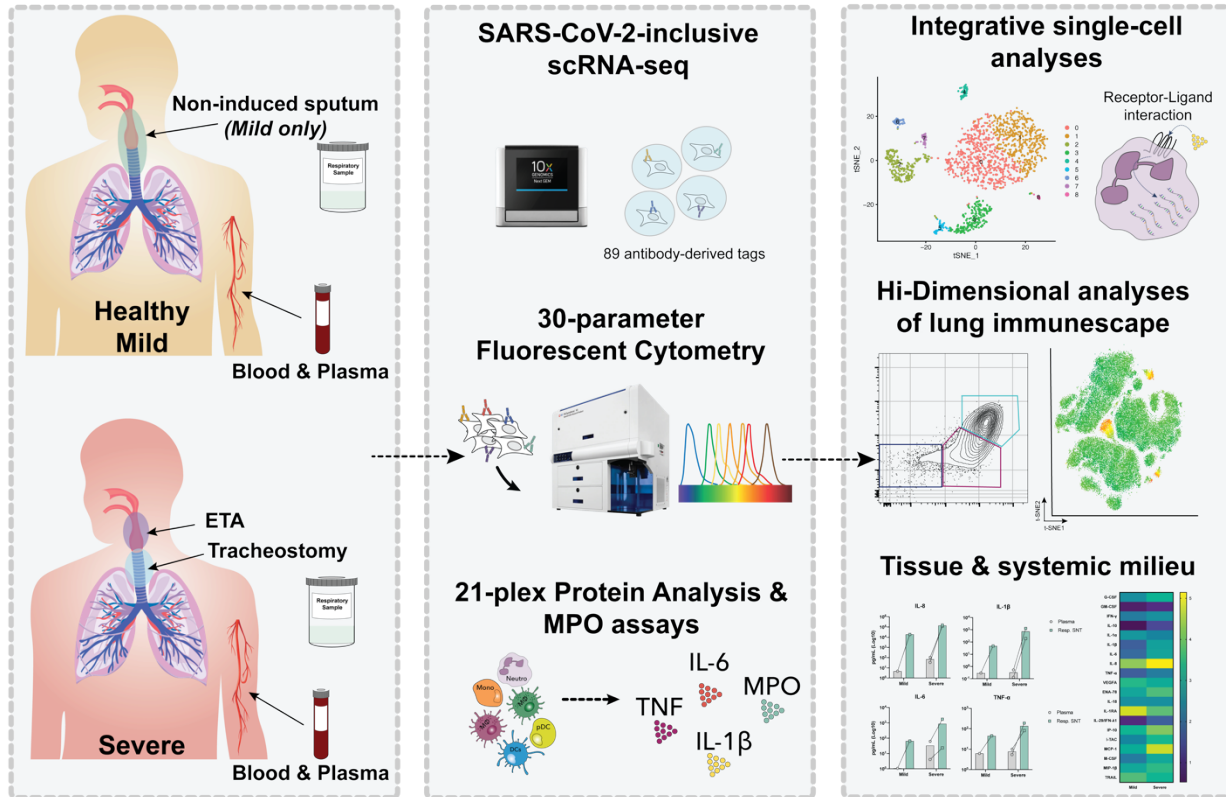
- 995  
996 78. Orlov, M. *et al.* Endotracheal aspirates contain a limited number of lower respiratory tract  
997 immune cells. *Critical Care* **25**, 1-3 (2021).  
998  
999 79. Seren, S. *et al.* Proteinase release from activated neutrophils in mechanically ventilated  
1000 patients with non-COVID-19 and COVID-19 pneumonia. *Eur Respir J* **57** (2021).  
1001  
1002 80. Dobin, A. *et al.* STAR: ultrafast universal RNA-seq aligner. *Bioinformatics* **29**, 15-21  
1003 (2013).  
1004  
1005 81. Hao, Y. *et al.* Integrated analysis of multimodal single-cell data. *bioRxiv* (2020).  
1006  
1007 82. Babcock, B.R., Kusters, A., Yang, J., White, M.L. & Ghosn, E. Data Matrix Normalization  
1008 and Merging Strategies Minimize Batch-specific Systemic Variation in scRNA-Seq Data.  
1009 *bioRxiv* (2021).  
1010  
1011 83. Mulè, M.P., Martins, A.J. & Tsang, J.S. Normalizing and denoising protein expression  
1012 data from droplet-based single cell profiling. *bioRxiv* (2020).  
1013  
1014 84. Petukhov, V. *et al.* dropEst: pipeline for accurate estimation of molecular counts in  
1015 droplet-based single-cell RNA-seq experiments. *Genome Biol* **19**, 78 (2018).  
1016  
1017 85. Zhou, Y. *et al.* Metascape provides a biologist-oriented resource for the analysis of  
1018 systems-level datasets. *Nat Commun* **10**, 1523 (2019).  
1019  
1020 86. Lu, R. *et al.* Genomic characterisation and epidemiology of 2019 novel coronavirus:  
1021 implications for virus origins and receptor binding. *Lancet* **395**, 565-574 (2020).  
1022  
1023



1024  
1025  
1026  
1027  
1028  
1029  
1030  
1031  
1032  
1033  
1034  
1035

### Graphical Abstract

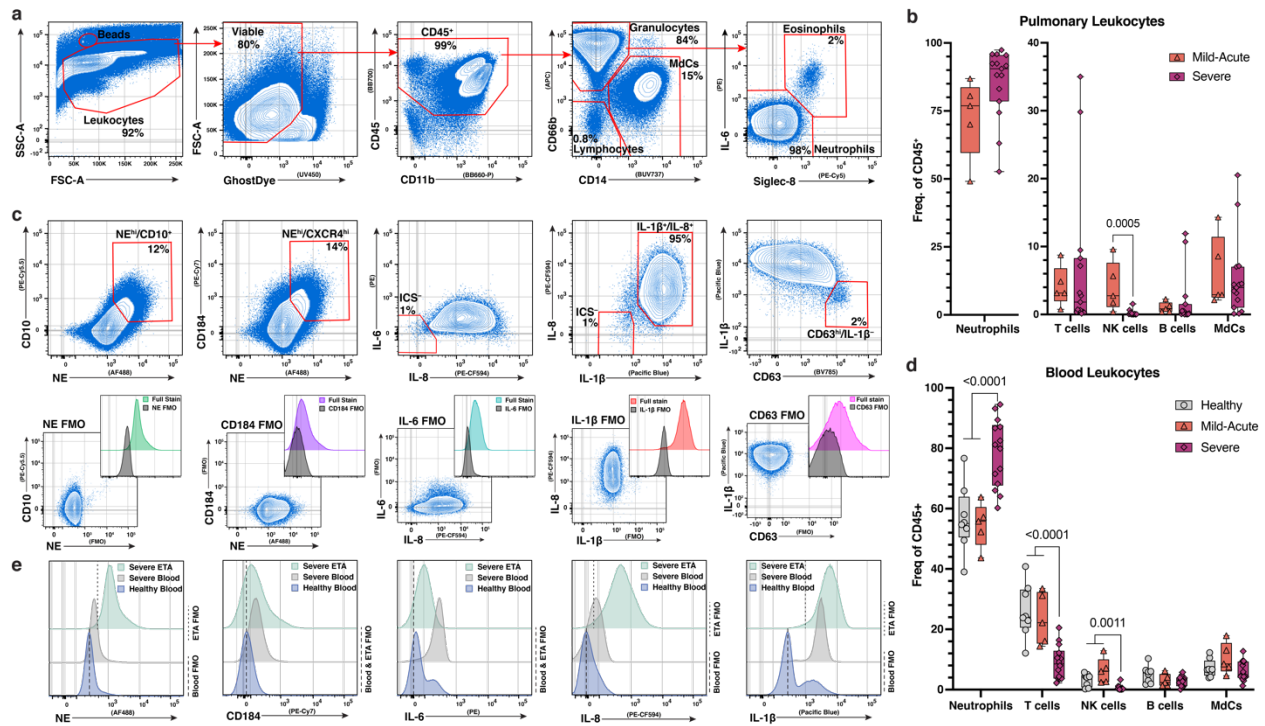
The lung pathology due to severe COVID-19 is marked by a perpetual pathogenic neutrophilia, leading to acute respiratory distress syndrome (ARDS) even in the absence of viral burden. Circulating mature neutrophils are recruited to the airways via IL-8 (CXCL8)/CXCR2 chemotaxis. Recently migrated neutrophils further differentiate into a transcriptionally active and hyperinflammatory state, with an exacerbated expression of IL-8 (CXCL8), IL-1 $\beta$  (*IL1B*), *CCL3*, *CCL4*, neutrophil elastase (NE), and myeloperoxidase (MPO) activity. Airway neutrophils and recruited inflammatory monocytes further increase their production of IL-8 (CXCL8), perpetuating lung neutrophilia in a feedforward loop. MDCs and T cells produce IL-1 $\beta$  and TNF, driving neutrophils reprogramming and survival.



1036  
1037  
1038  
1039  
1040  
1041  
1042  
1043  
1044  
1045  
1046  
1047  
1048  
1049

**Figure 1. Experimental design for the systems immunology approach (integrated multi-omics single-cell assays) to study COVID-19 patient samples.** Respiratory samples (sputum or endotracheal aspirates) and matching blood from all subjects were collected for analysis by 21-plex Mesoscale analysis, high-dimensional (Hi-D) 30-parameter flow cytometry, and multi-omics scRNA-seq. Cells from endotracheal aspirates (ETA) and blood of severe COVID-19 patients along with blood from healthy individuals were surface-stained with a panel of 89 oligo-conjugated monoclonal antibodies before single-cell encapsulation, and analyses were performed with a custom human reference genome that included the SARS-CoV-2 genome to simultaneously detect viral mRNA transcripts. Integrative multi-omics analyses were performed on the resulting data sets.

1050



1051

1052

1053

1054

1055

1056

1057

1058

1059

1060

1061

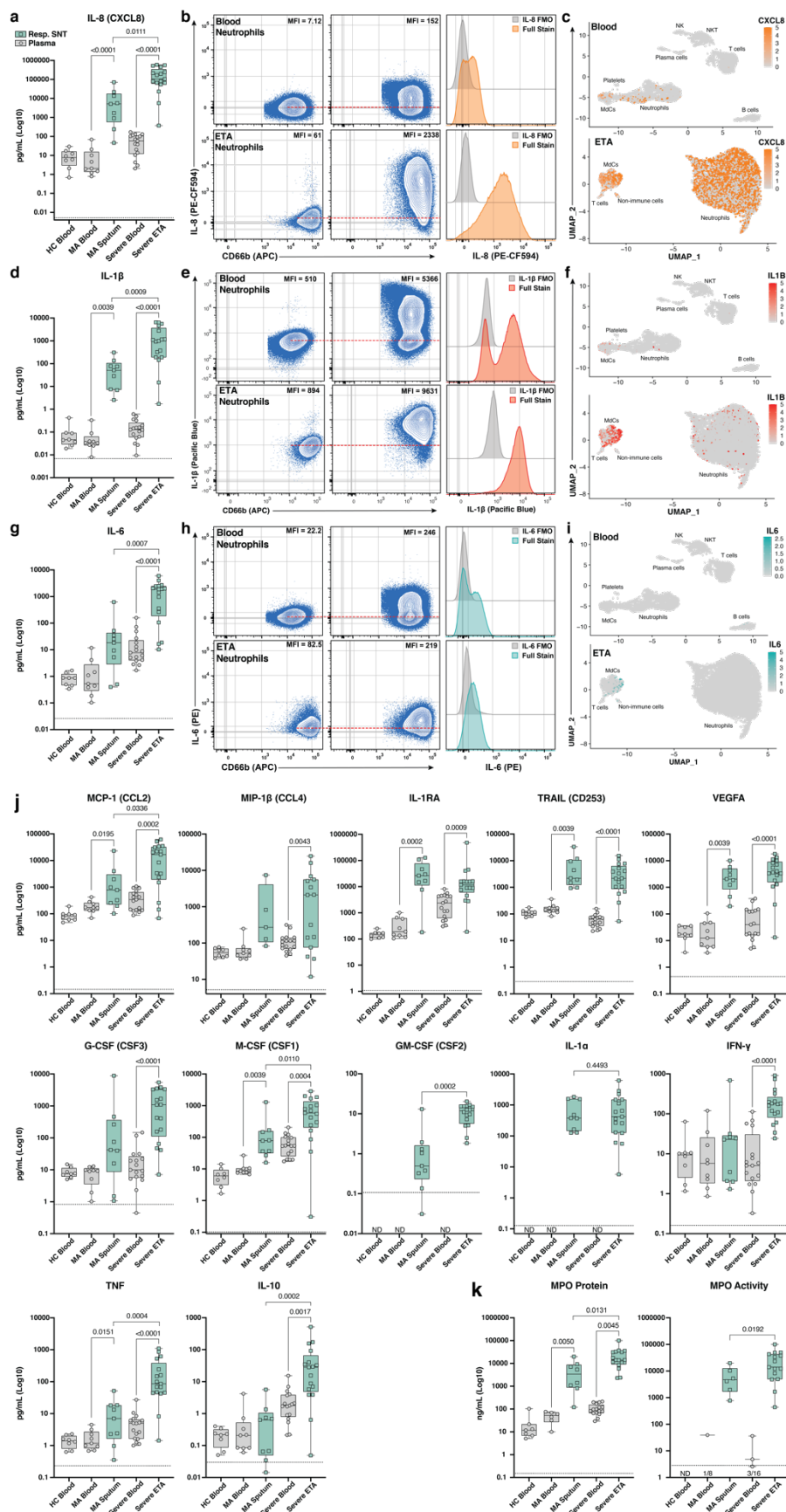
1062

1063

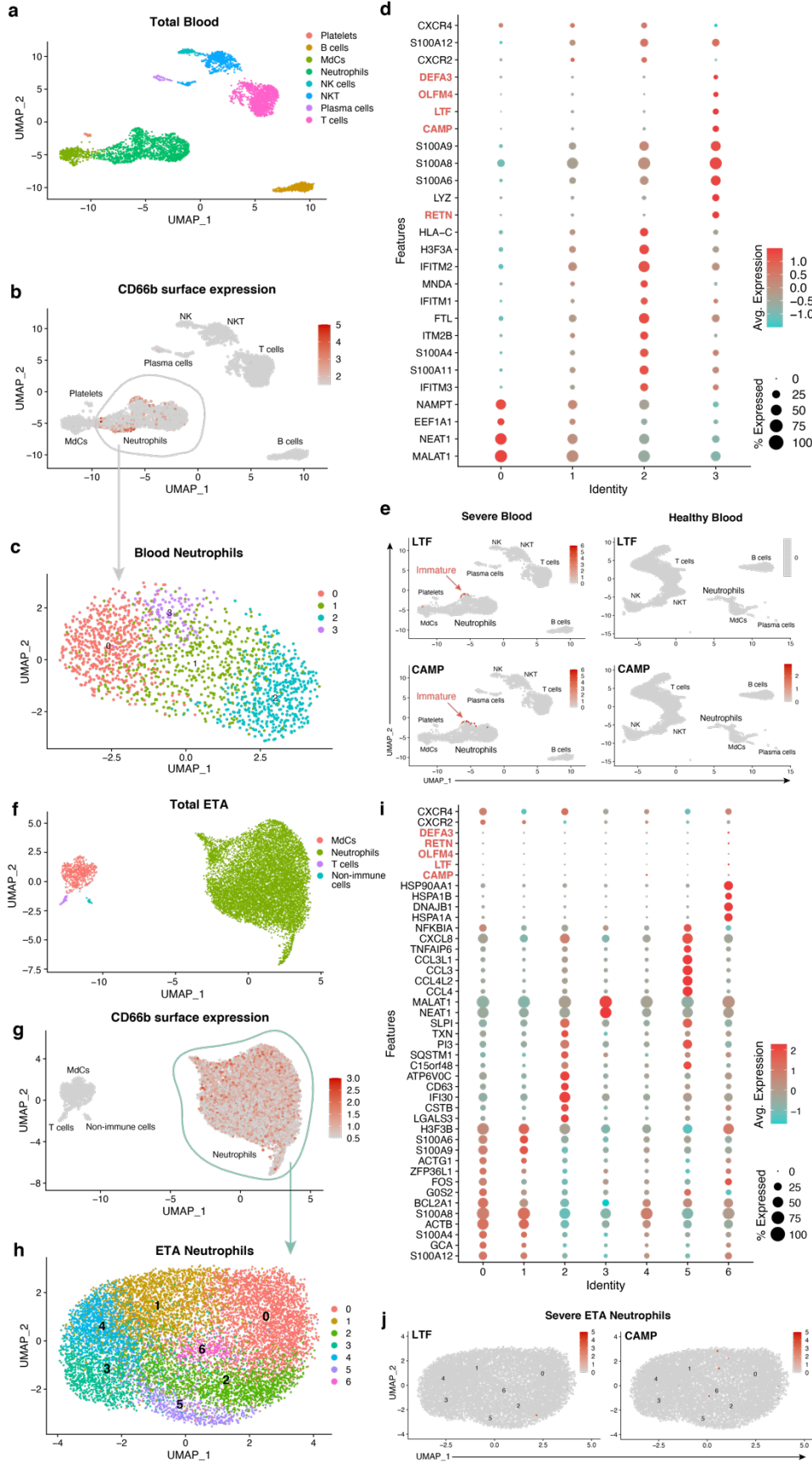
1064

1065

**Figure 2. Exacerbated neutrophilia in the airways and matching blood of severe COVID-19 patients.** (a) Representative gating strategy for all samples (see Extended Data Fig. 1 for full gating strategy). (b) Box plots show distributions of leukocytes isolated from endotracheal aspirates (ETA). (c) Representative plots demonstrating inflammatory profile of pulmonary neutrophils including neutrophil elastase (NE), CD184 (CXCR4), and intracellular staining of IL-6, IL-8, and IL-1 $\beta$  including the full stain and fluorescence minus one (FMO) controls (d) Box plots show distributions of leukocytes isolated from whole blood from severe patients. (e) Representative histograms showing median fluorescence intensity (MFI) of key markers across healthy blood (blue), severe blood (gray), and severe ETA (green) samples. MdCs = myeloid-derived cells. For comparisons across the three patient groups (i.e., healthy, mild-acute, severe), ordinary one-way ANOVA (if equal variance) or Brown-Forsythe and Welch ANOVA (if unequal variance) tests were performed for data with a normal distribution. Data with a lognormal distribution were analyzed with a Kruskal-Wallis test.



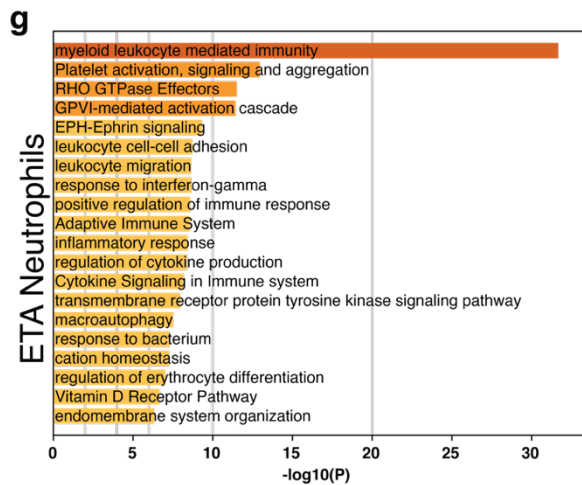
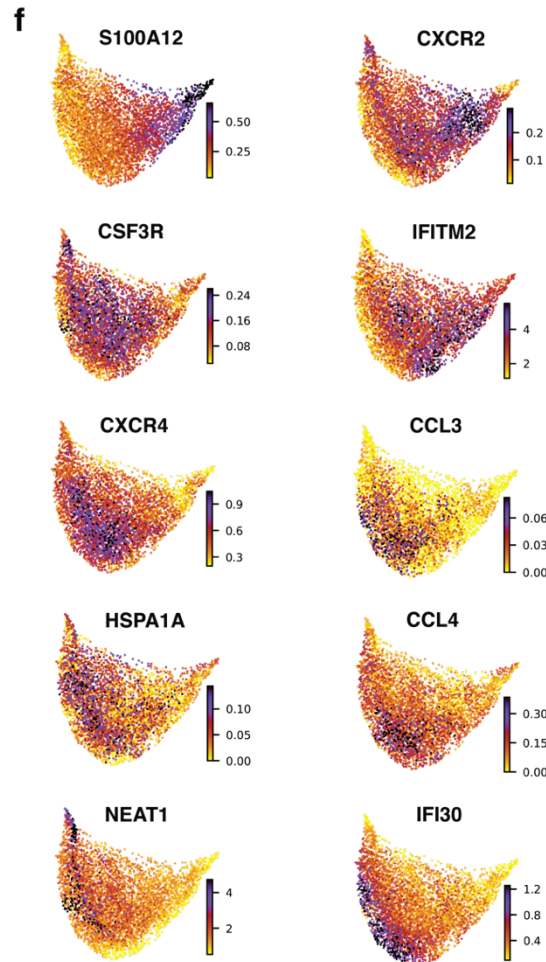
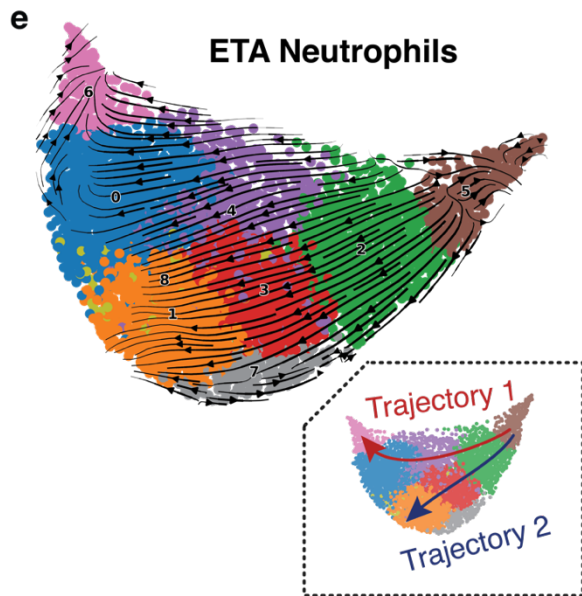
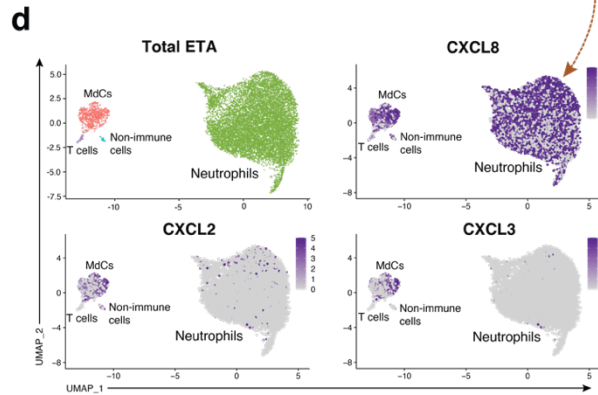
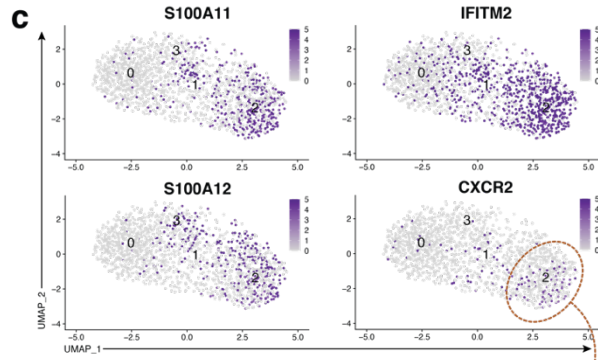
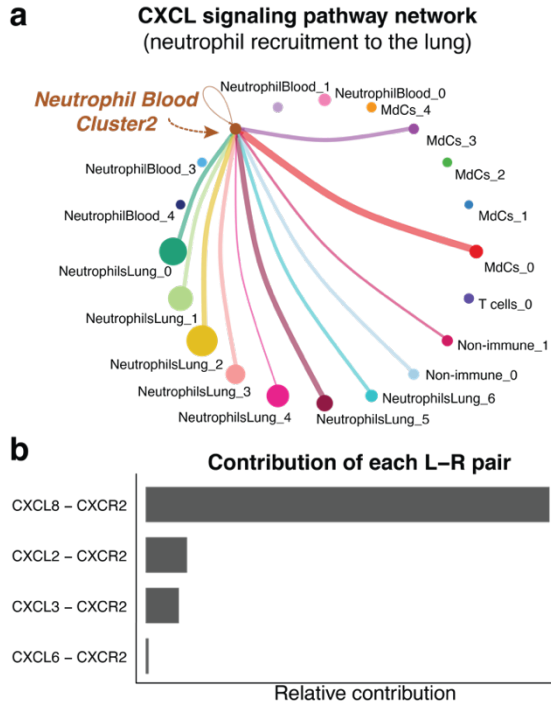
1067 **Figure 3. Cytokine release syndrome is dominated by IL-8 and IL-1 $\beta$  with pronounced**  
1068 **myeloperoxidase content and activity in the lung microenvironment.** (a, d, g, j)  
1069 Concentration (pg/mL) of 15 analytes interrogated by Mesoscale analyses in plasma (gray  
1070 circles) and respiratory supernatant (Resp. SNT; green squares) from healthy control (HC),  
1071 mild-acute (MA), and severe COVID-19 patients. (b, e, h) Representative flow cytometric  
1072 intracellular staining for IL-8 (CXCL8), IL-1 $\beta$ , and IL-6, including the full stain and fluorescence  
1073 minus one (FMO) controls in both blood and ETA neutrophils (CD66b<sup>+</sup>). (c, f, i) UMAP  
1074 visualizations of *CXCL8* (IL-8), *IL1B*, and *IL6*, which were also measured by intracellular flow  
1075 cytometry staining and Mesoscale in both blood and ETA. (k) Concentration (ng/mL) of  
1076 myeloperoxidase (MPO) protein and MPO activity in plasma vs. Resp. SNT. In (a, d, g, j, k),  
1077 black dotted line = median lower limit of detection (LLOD) for assays (see Extended Data Table  
1078 3). In (b, e, h) red dashed line indicates the median fluorescence intensity (MFI) of neutrophils in  
1079 the FMO control (value listed in the plot).  
1080



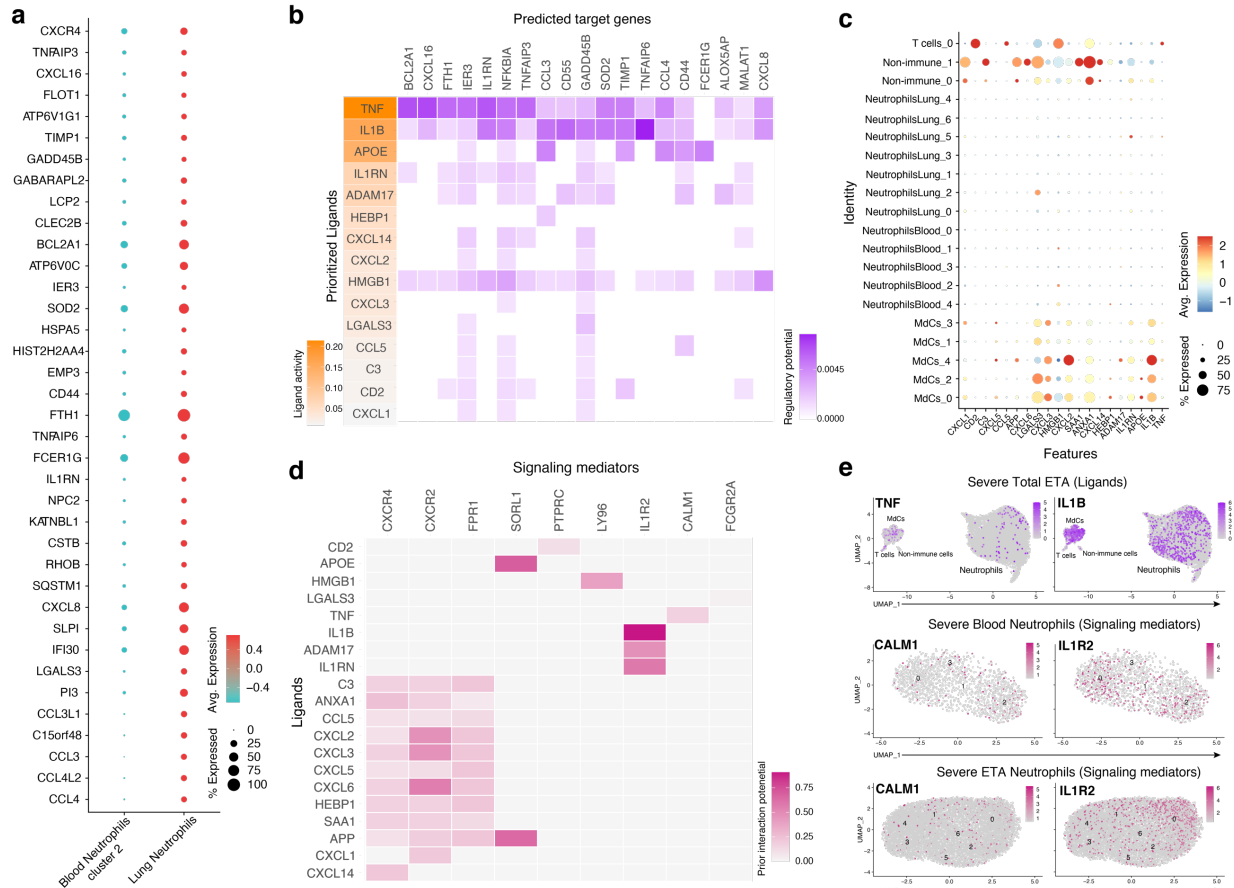


1082 **Figure 4. Multi-omic single-cell RNA-seq reveals emergency granulopoiesis in the**  
1083 **circulation and abundant heterogeneous populations of mature neutrophils in the**  
1084 **airways with distinct inflammatory states.** UMAP visualization of scRNA-seq of total  
1085 integrated blood (a) and endotracheal aspirate (ETA) (f) cells. Neutrophils were identified based  
1086 on cell-surface markers (b and g), and total neutrophils were subclustered for further analysis (c  
1087 and h). Dot plots of the intersection of the top differentially expressed genes in neutrophil  
1088 clusters (d and i) sorted by average log-fold change for blood (d) and lung (i) neutrophils,  
1089 respectively. UMAP visualization of signature genes of immature neutrophils (highlighted in d  
1090 and i) in blood from severe patients compared to healthy individuals (e) and lungs of severe  
1091 patients (j).  
1092

1093



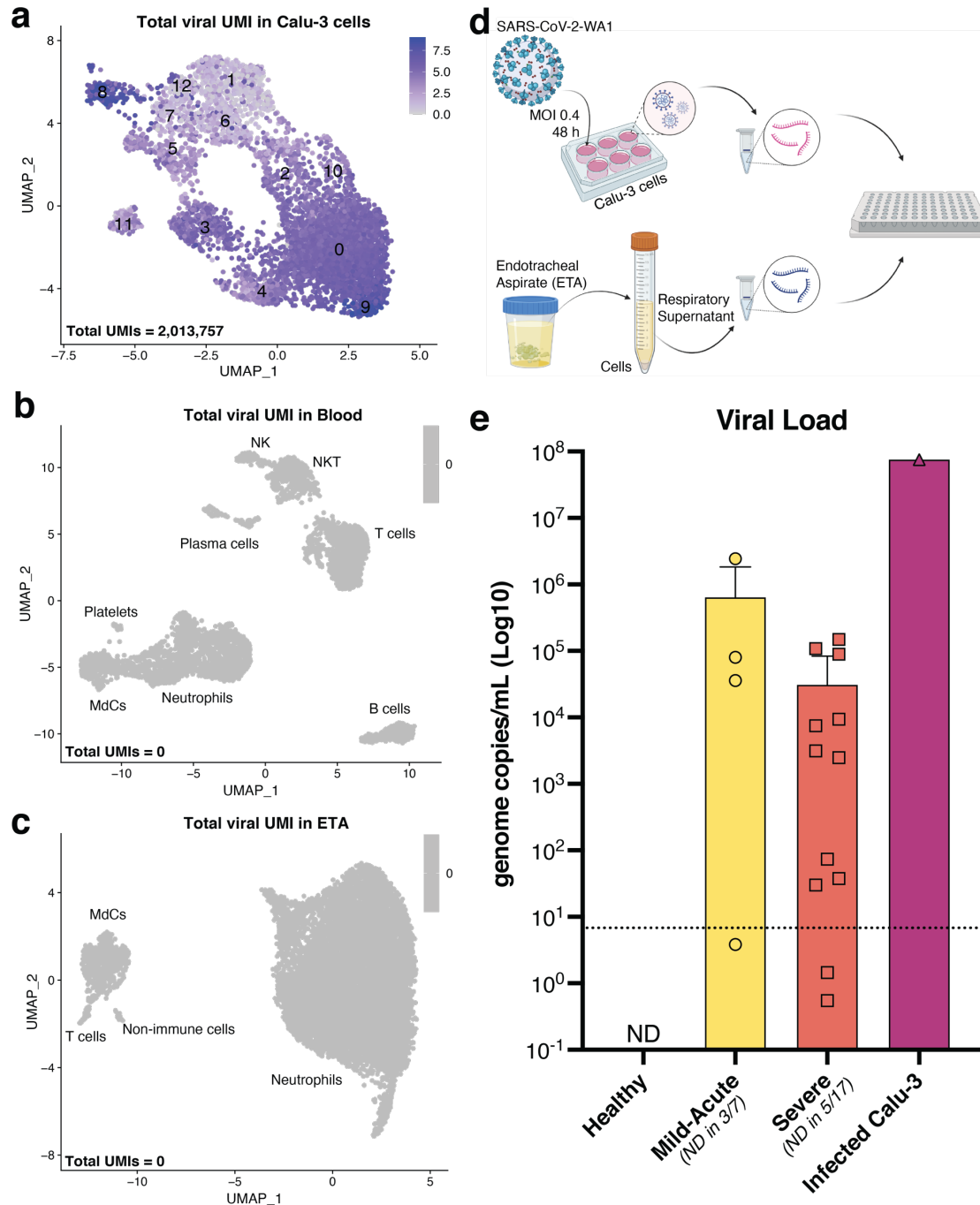
1094 **Figure 5. Mature neutrophils are continuously recruited from circulation and progress**  
1095 **toward a hyperinflammatory state.** Cell receptor-ligand pair analyses (CellChat<sup>31</sup>) from  
1096 scRNA-seq data identify significant CXCL signaling pathway network enrichment between lung  
1097 cells and blood neutrophils (a and b). Blood neutrophil cluster 2 represents the main subset  
1098 potentially recruited to the lung (a). Recruitment of blood cluster 2 (a and c) is largely  
1099 orchestrated by the CXCL8 (IL-8)/CXCR2 axis, and to a lesser extent, by the CXCL2 and  
1100 CXCL3 (b and d). *S100A11/12*, *IFITM2*, and *CXCR2* mark a cluster of mature neutrophils in the  
1101 blood (c) that likely represents the neutrophil subset recruited to the lung (d). Cell trajectory  
1102 analysis (scVelo<sup>32</sup>) identifies two potential pathways (Trajectories 1 and 2) for recently migrated  
1103 neutrophils (e), that begin with a gene signature consistent with neutrophil blood cluster 2 (c and  
1104 f). Neutrophils recruited to the lung acquire a hyperinflammatory profile along Trajectory 2 (e  
1105 and f), characterized by high expression of interferon-stimulated gene (ISG) *IFI30* along with  
1106 macrophage inflammatory proteins *CCL3* (MIP-1 $\alpha$ ) and *CCL4* (MIP-1 $\beta$ ), whereas *CSF3R* and  
1107 *CXCR4* are increased in cells along both trajectories (f). Neutrophils along Trajectory 1 may  
1108 reflect cells progressing to apoptosis expressing higher levels of *HSPA1A* (HSP70) followed by  
1109 *NEAT1* (f). Pathway and process enrichment analyses performed in Metascape<sup>85</sup> reveals that  
1110 myeloid-mediated immunity and platelet activation, signaling, and aggregation are significantly  
1111 enriched in neutrophils in the lungs of severe patients (g). MdCs: Myeloid-derived Cells.  
1112



1113  
1114  
1115  
1116  
1117  
1118  
1119  
1120  
1121  
1122  
1123  
1124  
1125  
1126

**Figure 6. *TNF* and *IL-1 $\beta$*  drive inflammatory program in neutrophils recruited to the lung.**

(a) Dot plots showing 37 of the 67 differentially expressed genes in lung neutrophils versus blood neutrophil cluster 2 sorted by average log-fold change used as input for NicheNet<sup>38</sup> analyses (b) NicheNet<sup>38</sup> analyses identified the highest prioritized ligands (top 15) ordered by ligand activity (y-axis) that best predict the pulmonary neutrophil gene signature (x-axis). The predicted target genes represent the pulmonary neutrophil gene signature identified by differential gene expression analysis between blood neutrophils from cluster 2 and ETA neutrophils (see Extended Data Fig. 5d) (b) Dot plots of the intersection of the top 15 expressed prioritized ligands from all cells in the ETA samples. (c) Ligand-receptor matrix of putative signaling mediators for the top 15 prioritized ligands identified in (a). (d) UMAP visualizations of *TNF* and *IL1B* transcripts in the total ETA along with expression of predicted signaling mediators in blood (middle) and ETA (bottom) neutrophils from severe patients.



1127  
1128  
1129  
1130  
1131  
1132  
1133  
1134  
1135  
1136  
1137

**Figure 7. Viral transcripts (scRNA-seq) and viral load in the airways of severe patients.** Calu-3 cells infected with SARS-CoV-2 USA-WA1/2020 (MOI 0.4) were encapsulated for scRNA-seq assays (a) following the same protocol used for patient cells from blood (b) and ETA (c). Millions of viral transcripts (or unique molecular identifiers; UMIs) were detected in about 5,000 Calu-3 cells (a), but not in the cells from severe patients (total UMI = 0; b and c). RT-qPCR (d) results of culture supernatant from Calu-3 infected cells and respiratory supernatants from mild-acute and severe patients (e) show a lower viral load in severe patients than in mild-acute patients and in the Calu-3-infected culture supernatant. ND = not detected; horizontal dotted line = lower limit of detection (LLOD).

1138 **Supplemental Material:**

#	Demographic	PID	Status	Sex	Age Group	Dexamethasone or equivalent	Remdesivir (No. of doses)	Date PCR positive Dx	Date intubated	Date sample collected	Length ICU stay (days)	Clinical Outcome
1	AA	PHA0001	Severe	Male	35-54	Yes	0	6/9/2020	6/8/2020	6/17/2020	32	Recovered
2	AA	PHA0004	Severe	Male	35-54	Yes	0	7/11/2020	7/18/2020	8/5/2020	37	Recovered
3	AA	PHA0006	Severe	Male	35-54	Yes	0	8/11/2020	8/16/2020	8/20/2020	8	Recovered
4	AA	PHA0018	Severe	Male	35-54	Yes	2	10/14/2020	9/29/2020	10/8/2020	13	Recovered
5	AA	PHA0041	Severe	Male	35-54	Yes	2	2/6/2021	2/6/2021	2/10/2021	14	Recovered
6	AA	PHA0003	Severe	Male	55+	Yes	2	6/23/2020	6/25/2020	6/30/2020	14	Succumbed
7	A	PHA0008	Severe	Male	55+	Yes	2	8/29/2020	8/30/2020	9/3/2020	19	Recovered
8	AA	PHA0024	Severe	Male	55+	Yes	2	12/27/2020	12/31/2020	1/6/2021	9	Recovered
9	AA	PHA0025	Severe	Male	55+	Yes	0	12/20/2020	12/24/2020	1/8/2021	26	Recovered
10	AA	PHA0031	Severe	Male	55+	Yes	1	1/23/2021	1/24/2021	1/27/2021	11	Succumbed
11	AA	PHA0032	Severe	Male	55+	Yes	1	1/9/2021	1/14/2020	1/27/2021	40	Recovered
12	AA	PHA0035	Severe	Male	55+	Yes	0	1/18/2021	1/20/2021	2/2/2021	53	Recovered
13	AA	PHA0036	Severe	Female	18-34	Yes	2	1/10/2021	12/31/2020	2/2/2021	42	Recovered
14	AA	PHA0002	Severe	Female	55+	Yes	0	6/20/2020	6/20/2020	6/24/2020	25	Recovered
15	AA	PHA0005	Severe	Female	55+	Yes	0	7/16/2020	7/18/2020	8/12/2020	33	Recovered
16	AA	PHA0007	Severe	Female	55+	Yes	0	8/9/2020	8/10/2020	9/2/2020	60	Recovered
17	AA	PHA0010	Severe	Female	55+	Yes	2	9/17/2020	9/21/2020	9/24/2020	18	Recovered
18	AA	PHA0026	Severe	Female	55+	Yes	1	12/27/2020	12/28/2020	1/8/2021	16	Succumbed
19	A	PHA0040	Mild-Acute	Male	35-54	Yes	0	1/6/2021	N/A	2/8/2021	N/A	Recovered
20	AA	PHA0043	Mild-Acute	Male	35-54	Yes	0	Unclear	N/A	2/18/2021	N/A	Recovered
21	AA	PHA0023	Mild-Acute	Male	55+	Yes	0	11/6/2020	N/A	11/11/2020	N/A	Recovered
22	AA	PHA0047	Mild-Acute	Male	55+	Yes	0	2/8/2021	N/A	2/19/2021	N/A	Recovered
23	AA	PHA0012	Mild-Acute	Female	35-54	Yes	0	9/18/2020	N/A	9/29/2020	N/A	Recovered
24	AA	PHA0013	Mild-Acute	Female	35-54	Yes	0	9/21/2020	N/A	9/29/2020	N/A	Recovered
25	AA	PHA0044	Mild-Acute	Female	35-54	Yes	0	2/16/2021	N/A	2/19/2021	N/A	Recovered
26	AA	PHA0046	Mild-Acute	Female	35-54	Yes	0	2/12/2021	N/A	2/19/2021	N/A	Recovered
27	AA	PHA0045	Mild-Acute	Female	55+	Yes	0	2/12/2021	N/A	2/19/2021	N/A	Recovered
28	AA	PHA1009	Healthy	Female	18-34	Yes	0	N/A	N/A	10/23/2020	N/A	N/A
29	AA	PHA1005	Healthy	Female	35-54	Yes	0	N/A	N/A	10/23/2020	N/A	N/A
30	AA	PHA1006	Healthy	Female	35-54	Yes	0	N/A	N/A	10/23/2020	N/A	N/A
31	AA	PHA1007	Healthy	Female	35-54	Yes	0	N/A	N/A	10/23/2020	N/A	N/A
32	AA	PHA1008	Healthy	Female	35-54	Yes	0	N/A	N/A	10/23/2020	N/A	N/A
33	AA	PHA1010	Healthy	Female	35-54	Yes	0	N/A	N/A	10/23/2020	N/A	N/A
34	AA	PHA1011	Healthy	Female	35-54	Yes	0	N/A	N/A	2/10/2021	N/A	N/A
35	AA	PHA1012	Healthy	Female	55+	Yes	0	N/A	N/A	2/17/2021	N/A	N/A

1139

1140 **Extended Data Table 1. Demographic and clinical data from the 35 Black/African**

1141 **American individuals enrolled in our studies.** Table describing demography, status, sex, and  
 1142 age of study participants along with select details of clinical course including administration of  
 1143 Dexamethasone and Remdesivir, date first intubated (severe, ICU patients only), date of PCR  
 1144 positive diagnosis (Dx), date clinical specimens were collected, and total length ICU stay in  
 1145 days, and clinical outcome (whether recovered or succumbed to disease).

1146

Characteristics	All subjects (N = 35)		
	Healthy (N = 8)	Mild-Acute (N=9)	Severe (N=18)
<b>Age</b>			
A. Mean age ± SD	46 ± 11	51 ± 12	56 ± 14
B. Age range	31 – 70	35 – 68	22 – 81
<b>Gender</b>			
A. Female	8 (100%)	5 (56%)	6 (33%)
B. Male	0 (0%)	4 (44%)	12 (67%)
<b>Site of endotracheal aspiration</b>			
A. Endotracheal tube	—	—	9 (50%)
B. Tracheostomy	—	—	9 (50%)
<b>Medical History</b>			
A. Smoking History			
i) Never	7 (87.5%)	7 (78%)	12 (67%)
ii) Former	1 (12.5%)	2 (22%)	2 (11%)
iii) Current	0 (0%)	0 (0%)	4 (22%)
B. Hypertension (HTN)	3 (37.5%)	3 (33%)	11 (61%)
C. Obesity	2 (25%)	1 (11%)	4 (22%)
D. Asthma	2 (25%)	2 (22%)	2 (11%)
E. COPD	0 (0%)	0 (0%)	2 (11%)
F. Diabetes mellitus (DM)			
i) Type I DM	0 (0%)	0 (0%)	0 (0%)
ii) Type II DM	1 (12.5%)	0 (0%)	8 (44%)
G. Deep vein thrombosis (DVT)	0 (0%)	0 (0%)	1 (5%)
H. Hypothyroidism	0 (0%)	0 (0%)	1 (5%)
I. Congestive Heart Failure (CHF)	1 (12.5%)	0 (0%)	5 (28%)
J. Gastroesophageal reflux disease (GERD)	1 (12.5%)	1 (11%)	1 (5%)
K. Dyslipidemia	0 (0%)	1 (11%)	1 (5%)
L. Obstructive sleep apnea (OSA)	0 (0%)	0 (0%)	2 (11%)
M. Coronary artery disease (CAD)	0 (0%)	0 (0%)	1 (5%)
N. Chronic kidney disease	0 (0%)	1 (11%)	1 (5%)
O. Cancer	0 (0%)	0 (0%)	0 (0%)
P. Autoimmune hemolytic anemia	0 (0%)	0 (0%)	1 (5%)
Q. Thrombocytopenia	0 (0%)	0 (0%)	1 (5%)
R. Arthritis/Rheumatoid arthritis (RA)	1 (12.5%)	0 (0%)	1 (5%)
<b>Complications</b>			
A. Acute respiratory distress syndrome (ARDS)	—	—	18 (100%)
B. Hypoxemic respiratory failure	—	—	13 (72%)
C. Extracorporeal membrane oxygenation (ECMO)	—	—	2 (11%)
D. Shock	—	—	15 (83%)
E. Nosocomial pneumonia	—	—	6 (33%)
F. Coagulopathy	—	—	3 (17%)
G. Seizures	—	—	3 (17%)
H. Cardiac arrhythmia	—	—	3 (17%)
I. Renal failure	—	—	8 (44%)
J. Renal replacement therapy	—	—	6 (33%)

1148 **Extended Data Table 2. *Clinical characteristics of the 35 Black/African American***  
1149 ***individuals enrolled in our studies.*** Table describing clinical characteristics of 35 patients  
1150 across the 3 cohorts (healthy, mild-acute, and severe) including age, gender, site of  
1151 endotracheal aspiration (ETA), medical history, along with complications for the severe patients  
1152 admitted to the ICU.  
1153



1154

**a** CoV-Neutrophil

Laser	Detector	Antigen	Fluorophore	Clone	Isotype	Vendor	Cat. No.	Titration
	B 488/10	Side Scatter (SSC)	—	—	—	—	—	—
1	B 515/20	Neutrophil elastase (NE)	AF488	950318	Mouse IgG1, κ	R&D Systems	IC91671G	1:25
2	B 610/20	CD45-RA	BB630-P	HI-100	Mouse IgG2a, κ	BD Biosciences	624294	1:160
3	488 nm B 670/30	CD11b	BB660-P	ICRF44	Mouse IgG1, κ	BD Biosciences	624295	1:50
4	B 710/50	CD45	BB700	HI-30	Mouse IgG1, κ	BD Biosciences	746090	1:640
5	B 750/30	CD4	BB755-P	RPA-T4	Mouse IgG1, κ	BD Biosciences	624391	1:100
6	B 780/60	HLA-DR (MHC II)	BB790-P	G46-6	Mouse IgG2a, κ	BD Biosciences	624296	1:50
7	V 431/28	CD163	BV421	GHI/6I	Mouse IgG1, κ	BioLegend	333612	1:25
8	V 470/15	IL-1β	Pacific Blue	H1b-98	Mouse IgG1, κ	BioLegend	511710	1:20
9	V 586/15	CD56	BV570	HCD56	Mouse IgG1, κ	BioLegend	318330	1:100
10	405 nm V 610/20	CD86 *	BV605	FUN-1	Mouse IgG1, κ	BD Biosciences	562999	1:50
11	V 670/30	TNF	BV650	MAb11	Mouse IgG1, κ	BD Biosciences	563418	1:80
12	V 710/50	CD19	BV711	HIB19	Mouse IgG1, κ	BioLegend	302246	1:20
13	V 740/35	CD16 (FcγRIII)	BV750	3G8	Mouse IgG1, κ	BD Biosciences	747461	1:320
14	V 780/60	CD63 (LAMP-3)	BV785	H5C6	Mouse IgG1, κ	BioLegend	353044	1:80
15	YG 586/15	IL-6	PE	MQ2-13A5	Rat IgG1, κ	BD Biosciences	554545	1:20
16	YG 610/20	IL-8 (CXCL8)	PE-CF594	G265-8	Mouse IgG2b, κ	BD Biosciences	563531	1:20
17	561 nm YG 670/30	Siglec-8 *	PE-Cy5	7C9	Mouse IgG1, κ	BioLegend	347114	1:100
18	YG 710/50	CD10	PE-Cy5.5	HI10a	Mouse IgG1, κ	Homemade	—	1:40
19	YG 780/60	CD184 *	PE-Cy7	12G5	Mouse IgG2a, κ	BioLegend	306514	1:40
20	UV 379/28	CD64 (FcγRI)	BUV395	10.1	Mouse IgG1, κ	BD Biosciences	740300	1:80
21	UV 450/50	GhostDye (Viability)	UV450	—	—	Tonbo Biosciences	13-0868-T500	1:100
22	355 nm UV 586/15	CD172a/b (SIRPα/β1)	BUV563	SE5A5	Mouse IgG1, κ	BD Biosciences	748435	1:10
23	UV 670/30	CD123 (IL-3Rα)	BUV661	9F5	Mouse IgG1, κ	BD Biosciences	741628	1:40
24	UV 740/35	CD14	BUV737	M5E2	Mouse IgG2a, κ	BD Biosciences	612763	1:50
25	UV 820/60	CD3ε	BUV805	SK1	Mouse IgG1, κ	BD Biosciences	612889	1:40
26	R 670/30	CD66b	APC	QA17A51	Mouse IgG1, κ	BioLegend	396906	1:200
27	640 nm R 710/50	CD11c	AF700	Bu15	Mouse IgG1, κ	BioLegend	337220	1:200
28	R 780/60	CD32 (FcγRII)	APC-Fire750	FUN-2	Mouse IgG2b, κ	BioLegend	303220	1:400

\* = alternate reagents used in panel iterations (see c below); -P denotes prototype reagents

**b** CoV-Global Distributions

Laser	Detector	Antigen	Fluorophore	Clone	Isotype	Vendor	Cat. No.	Titration
	B 488/10	Side Scatter (SSC)	—	—	—	—	—	—
1	488 nm B 515/20	CD45	AF488	HI-30	Mouse IgG1, κ	BioLegend	304017	1:160
2	V 431/28	CD56	BV421	HCD56	Mouse IgG1, κ	BioLegend	318328	1:40
3	V 610/20	CD8α	BV605	SK1	Mouse IgG1, κ	BioLegend	344742	1:20
4	405 nm V 670/30	HLA-DR (MHC II)	BV650	L243	Mouse IgG2a, κ	BioLegend	307650	1:50
5	V 710/50	CD4	BV711	RPA-T4	Mouse IgG1, κ	BioLegend	300558	1:40
6	V 740/35	CD16 (FcγRIII)	BV750	3G8	Mouse IgG1, κ	BD Biosciences	747461	1:320
7	V 780/60	CD19	BV785	HIB19	Mouse IgG1, κ	BioLegend	302240	1:40
8	YG 586/15	CD123 (IL-3Rα)	PE	6H6	Mouse IgG1, κ	BioLegend	306006	1:400
9	561 nm YG 670/30	Siglec-8	PE-Cy5	7C9	Mouse IgG1, κ	BioLegend	347114	1:100
10	YG 710/50	CD14	PE-Fire700	63D3	Mouse IgG1, κ	BioLegend	367158	1:100
11	YG 780/60	CD11c	PE-Cy7	Bu-15	Mouse IgG1, κ	BioLegend	337216	1:160
12	355 nm UV 450/50	GhostDye (Viability)	UV450	—	—	Tonbo Biosciences	13-0868-T500	1:100
13	R 670/30	CD11b	APC	ICRF44	Mouse IgG1, κ	BioLegend	301350	1:400
14	640 nm R 710/50	CD3ε	AF700	HIT3a	Mouse IgG2a, κ	BioLegend	300324	1:320
15	R 780/60	CD66b	APC-Fire750	QA17A51	Mouse IgG1, κ	BioLegend	396908	1:80

**c** Alternate Reagents

Laser	Detector	Antigen	Fluorophore	Clone	Isotype	Vendor	Cat. No.	Titration
1	405 nm V670/30	CD169 (Siglec-1)	BV605	7-239	Mouse IgG1, κ	BioLegend	346010	1:40
2	V670/30	CD182 (CXCR2)	BV605	6C6	Mouse IgG1, λ	BD Biosciences	744197	1:40
3	561 nm YG 670/30	CD86	PE-Cy5	IT2.2	Mouse IgG1, κ	BioLegend	305408	1:20
4	YG 780/60	CD206 (MMR)	PE-Cy7	15-2	Mouse IgG2a, κ	BioLegend	321124	1:10

1155

1156 **Extended Data Table 3. *High-dimensional 30-parameter, including intracellular cytokine***  
1157 ***staining, and 17-parameter flow cytometry panels used for airway and blood cells.*** Flow  
1158 cytometer configuration and cytometry reagents used in the final panels to interrogate (a)  
1159 neutrophil phenotype and (b) global immune cell distributions and blood and ETA samples.  
1160 Channels marked with an asterisk (\*) denote alternate reagents (c) used in earlier panel  
1161 iterations for some samples in this study. Monoclonal antibody (mAb) master mixes were  
1162 prepared in BD Horizon™ Brilliant Stain Buffer and samples stained as described in the  
1163 methods section. Titrations of all reagents were determined in house for each lot independently  
1164 prior to use. AF: AlexaFluor, APC: Allophycocyanin, BB: Brilliant Blue, BUV: Brilliant Ultraviolet,  
1165 BV: Brilliant Violet, FITC: Fluorescein isothiocyanate, PE: Phycoerythrin. Fluorophores marked  
1166 with -P denote prototype reagents and are custom conjugations from BD Biosciences.  
1167

<b>a</b>	<b>Analyte</b>	<b>Median LLOD (pg/mL)</b>	<b>LLOD Range (pg/mL)</b>
1	G-CSF (CSF3)	0.84 ± 0.88	0.15—2.12
2	GM-CSF (CSF2)	0.11 ± 0.13	0.01—0.31
3	IFN-γ	1.31 ± 1.12	0.16—2.79
4	IL-10	0.03 ± 0.02	0.01—0.06
5	IL-1α	0.13 ± 0.07	0.04—0.19
6	IL-1β	0.07 ± 0.05	0.01—0.12
7	IL-6	0.31 ± 0.39	0.03—0.89
8	IL-8 (CXCL8)	0.03 ± 0.03	0.02—0.08
9	TNF	0.24 ± 0.13	0.07—0.35
10	VEGFA	0.43 ± 0.44	0.06—1.06
11	ENA-78 (CXCL5)	0.15 ± 0.07	0.08—0.23
12	IL-18	1.02 ± 1.31	0.14—2.92
13	IL-1RA	1.08 ± 0.23	0.83—1.28
14	IL-29 (IFNλ1)	0.28 ± 0.11	0.13—0.38
15	IP-10 (CXCL10)	0.70 ± 0.99	0.18—2.19
16	I-TAC (CXCL11)	1.82 ± 0.23	1.59—2.13
17	MCP-1 (CCL2)	0.14 ± 0.05	0.09—0.21
18	M-CSF (CSF1)	0.10 ± 0.04	0.06—0.14
19	MIP-1β (CCL4)	5.17 ± 2.40	2.78—8.51
20	TRAIL (CD253)	0.28 ± 0.11	0.18—0.44
21	SDF1α (CXCL12)	30.13 ± 26.73	10.60—60.60

<b>b</b>	<b>Assay</b>	<b>Median LLOD (ng/mL)</b>	<b>LLOD Range (ng/mL)</b>	<b>Median LLOQ (ng/mL)</b>	<b>LLOQ Range (ng/mL)</b>
1	Total MPO	0.15 ± 0.15	0.03—0.42	0.30 ± 0.30	0.05—0.84
2	MPO Activity	2.86 ± 1.98	0.38—6.03	5.72 ± 3.96	0.76—12.07

1168

1169

1170

1171

1172

1173

1174

**Extended Data Table 4. Mesoscale U-PLEX biomarker group 1 human and myeloperoxidase (MPO) assays.** Median ± SD and range of lower limits of detection (LLOD) for (a) Mesoscale UPLEX analytes and (b) MPO assays. Lower limits of quantification (LLOQ; MPO assays) and LODs (determined by standard curve) were run for each assay plate independently and the median LLOD plotted as horizontal dotted lines for each assay (see Fig. 3 and Extended Data Fig. 2).

Antigen	Clone	Vendor	Cat. No.	Antigen	Clone	Vendor	Cat. No.
1 CD10	HI10a	Biologend	312233	46 CD324	67A4	Biologend	324127
2 CD101 (BB27)	BB27	Biologend	331017	47 CD326 (EpCAM)	9C4	Biologend	324247
3 CD103 (Integrin $\alpha$ E)	Ber-ACT8	Biologend	350233	48 CD335 (NKp46)	9.00E+02	Biologend	331941
4 CD107a (LAMP-1)	H4A3	Biologend	328649	49 CD370 (CLEC9A)	8F9	Biologend	353809
5 CD117 (c-kit)	104D2	Biologend	313243	50 CD38	HIT2	Biologend	303543
6 CD11b	ICRF44	Biologend	301359	51 CD4	RPA-T4	Biologend	300567
7 CD11c	S-HCL-3	Biologend	371521	52 CD40	5C3	Biologend	334348
8 CD123 (IL-3R $\alpha$ )	6H6	Biologend	306045	53 CD41	HIP8	Biologend	303739
9 CD127 (IL-7R $\alpha$ )	A019D5	Biologend	351356	54 CD44	BJ18	Biologend	338827
10 CD133	S16016B	Biologend	394007	55 CD45	2D1	Biologend	368545
11 CD137	4B4-1	Biologend	309839	56 CD45R	RA3-6B2	Biologend	103273
12 CD138 (Syndecan-1)	MI15	Biologend	356539	57 CD45RA	HI100	Biologend	304163
13 CD14	M5E2	Biologend	301859	58 CD45RO	UCHL1	Biologend	304259
14 CD15 (SSEA-1)	W6D3	Biologend	323053	59 CD49a	TS2/7	Biologend	328319
15 CD16 (Fc $\gamma$ RIII)	3G8	Biologend	302065	60 CD5	UCHT2	Biologend	300637
16 CD161	HP-3G10	Biologend	339947	61 CD56 (NCAM)	QA17A16	Biologend	392425
17 CD163	GHI/61	Biologend	333637	62 CD62L	DREG-56	Biologend	304851
18 CD169	7-239	Biologend	346021	63 CD64 (Fc $\gamma$ RI)	10.1	Biologend	305045
19 CD183 (CXCR3)	G025H7	Biologend	353747	64 CD66b	6/40c	Biologend	392909
20 CD184 (CXCR4)	12G5	Biologend	306533	65 CD69	FN50	Biologend	310951
21 CD185 (CXCR5)	J252D4	Biologend	356939	66 CD80	2D10	Biologend	305243
22 CD19	HIB19	Biologend	302265	67 CD86	IT2.2	Biologend	305447
23 CD196 (CCR6)	G034E3	Biologend	353440	68 CD8 $\alpha$	RPA-T8	Biologend	301071
24 CD197 (CCR7)	G043H7	Biologend	353251	69 CD95 (Fas)	DX2	Biologend	305651
25 CD1c	L161	Biologend	331547	70 CX3CR1	K0124E1	Biologend	355705
26 CD1d	51.1	Biologend	350319	71 HLA-DR	L243	Biologend	307663
27 CD20	2H7	Biologend	302363	72 IgD	IA6-2	Biologend	348245
28 CD206 (MMR)	15-2	Biologend	321147	73 IgG	M1310G05	Biologend	410727
29 CD209 (DC-SIGN)	9E9A8	Biologend	330121	74 IgM	MHM-88	Biologend	314547
30 CD21	Bu32	Biologend	354923	75 Ig light chain $\kappa$	MHK-49	Biologend	316533
31 CD23	EBVCS-5	Biologend	338525	76 Ig light chain $\lambda$	MHL-38	Biologend	316629
32 CD24	ML5	Biologend	311143	77 Siglec-8	7C9	Biologend	347115
33 CD25	BC96	Biologend	302649	78 TCR V $\alpha$ 7.2	3C10	Biologend	351735
34 CD269 (BCMA)	19F2	Biologend	357523	79 TCR $\gamma/\delta$	B1	Biologend	331231
35 CD27	O323	Biologend	302853	80 TIGIT (VSTM3)	A15153G	Biologend	372729
36 CD274 (PD-L1)	29E.2A3	Biologend	329751	81 XCR1	S15046E	Biologend	372617
37 CD275 (ICOSL)	2D3	Biologend	309419	<b>Custom oligo-conjugated in-house</b>			
38 CD279 (PD-1)	EH12.2H7	Biologend	329963	82 ACE2	535919	Sino Biological	MAB9332-100
39 CD28	CD28.2	Biologend	302963	83 CD160	BY55	Biologend	341202
40 CD29 (Integrin $\beta$ 1)	TS2/16	Biologend	303029	84 CD16b	2D2G5B9	Sino Biological	11046-MM01
41 CD3	UCHT1	Biologend	300479	85 CD178	NOK-1	Biologend	306402
42 CD307d (FcRL4)	413D12	Biologend	340213	86 CD34	581	Biologend	343602
43 CD307e (FcRL5)	509f6	Biologend	340309	87 CD43	CD43-10G7	Biologend	343202
44 CD309 (VEGFR2)	7D4-6	Biologend	359921	88 CD9	HI9a	Biologend	312102
45 CD32 (Fc $\gamma$ RII)	FUN-2	Biologend	303225	89 IgA	IS11-8E10	Mytenyi	130-093-073

1175  
1176  
1177  
1178  
1179  
1180  
1181  
1182  
1183  
1184  
1185  
1186

**Extended Data Table 5. Panel of oligo-conjugated antibodies used in multi-omics scRNA-seq assays to measure surface protein markers on cells from airways and blood.** A total of 89 oligo-conjugated antibody-derived tags (ADT) were used to evaluate surface protein expression of target antigens via scRNA-seq. Reagents no. 82-89 were not commercially available in the TotalSeq-C™ format (BioLegend), so custom oligo-conjugated reagents were generated in-house using purified monoclonal antibodies and commercially available 5' Feature Barcode Antibody Conjugation - Lightning-Link® kits (abcam). Titrations of all reagents were determined in-house for each lot independently prior to use. Cells were surface stained prior to encapsulation and surface marker expression of major lineage markers were used to help cluster/validate gene expression data as described in the methods.

		PID	Total reads	Mean reads/cell
ETA	GEX	PHA0007	593,835,060	350,345
		PHA0008	555,825,992	2,241,234
		PHA0010	587,153,474	872,442
		PHA0018	541,561,148	459,729
	ADT	PHA0007	85,070,531	2,101
		PHA0008	78,647,311	7,514
		PHA0010	46,042,783	2,989
		PHA0018	73,265,461	5,399
Blood	GEX	PHA0007	518,672,044	273,129
		PHA0008	540,400,013	641,044
		PHA0010	592,394,112	543,980
		PHA0018	556,699,985	1,484,533
		PHA1005	541,306,254	158,787
		PHA1006	501,896,927	200,198
		PHA1007	512,999,099	172,902
		PHA1008	506,988,059	160,898
		PHA1009	527,201,752	130,463
		PHA1010	480,796,663	332,042
	ADT	PHA0007	74,597,277	2,115
		PHA0008	80,175,737	1,536
		PHA0010	62,927,249	1,067
		PHA0018	79,818,668	1,395
		PHA1005	77,435,258	1,145
		PHA1006	88,850,369	1,334
		PHA1007	88,329,209	1,169
		PHA1008	93,579,790	1,351
PHA1009	91,162,676	1,281		
PHA1010	89,597,131	1,251		

1187  
1188  
1189  
1190  
1191  
1192  
1193

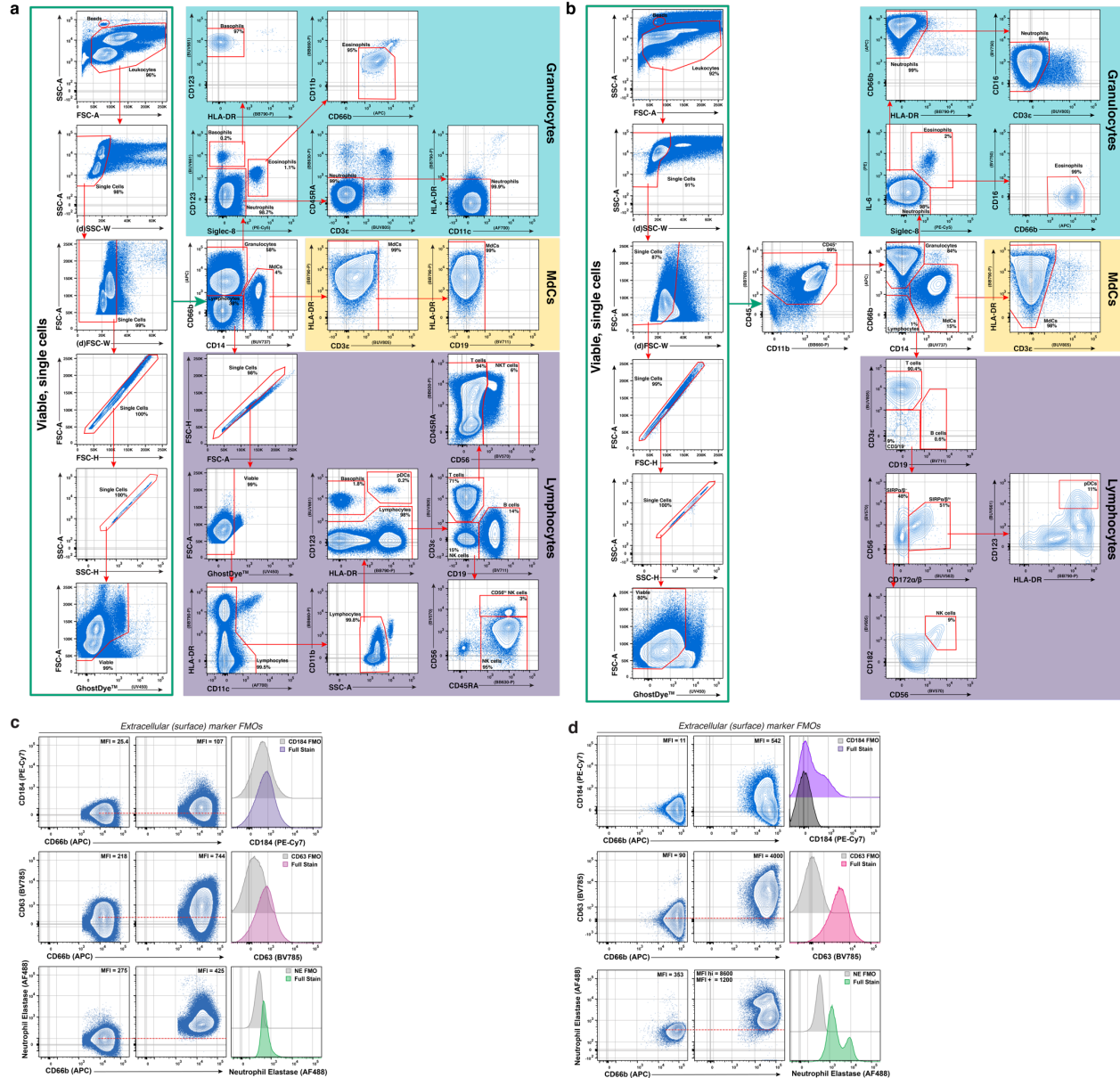
**Extended Data Table 6. Sequencing depth of independent samples.** All gene expression (GEX) libraries were pooled and run in a single S4 flow cell on a NovaSeq™ 6000. All antibody-derived tag (ADT) libraries were pooled and sequenced in a single lane of a S4 flow cell on a NovaSeq™ 6000. Total reads and mean number of reads per cell for GEX and ADT are reported independently for each sample, with an average read depth of 540,000,000 reads per sample (GEX) and 79,000,000 reads per sample (ADT).

<b>a</b>	<b>PID</b>	<b>Blood (%)</b>	<b>ETA (%)</b>
	PHA0007	30	30
	PHA0008	20	25
	PHA0010	10	25
	PHA0018	30	25
	PHA1005	30	
	PHA1006	30	
	PHA1007	30	
	PHA1008	20	
	PHA1009	20	
	PHA1010	25	

<b>b</b>	<b>PID</b>	<b>Total ADT UMI</b>	
		<b>Blood</b>	<b>ETA</b>
	PHA0007	125–500	125–1250
	PHA0008	125–1000	125–1250
	PHA0010	125–1500	125–750
	PHA0018	125–1500	125–1000
	PHA1005	125–1250	
	PHA1006	125–1250	
	PHA1007	125–1500	
	PHA1008	125–1500	
	PHA1009	125–1500	
	PHA1010	125–1500	

1194  
1195  
1196  
1197  
1198  
1199  
1200

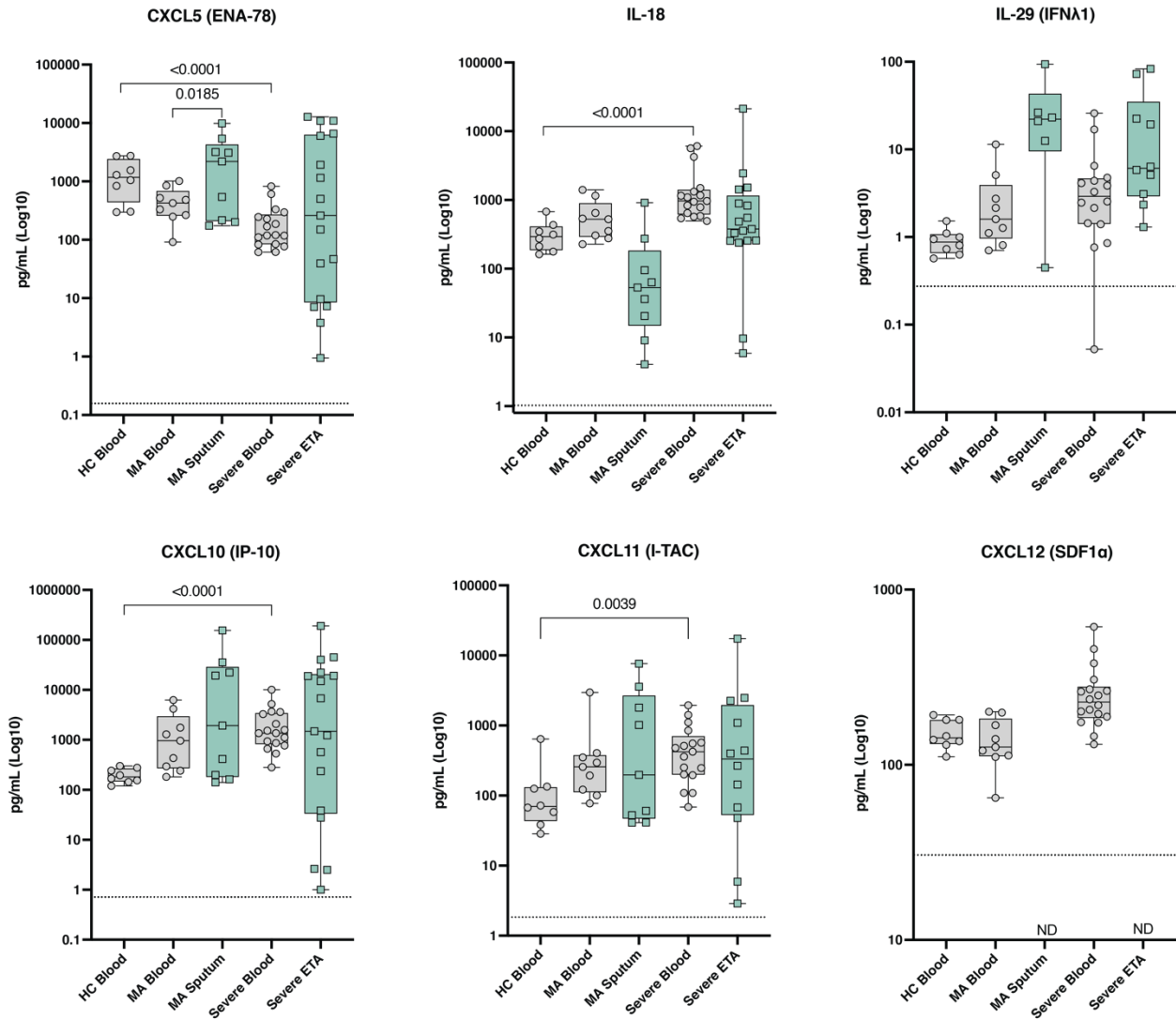
**Extended Data Table 7. Mitochondrial gene thresholds and total ADT UMIs of individual samples.** (a) Threshold for mitochondrial gene distribution (percentage) for each sample used to exclude potential dead cells in scRNA-seq data. Threshold was evaluated and set for each sample independently. (b) The distribution of total ADT UMIs was determined and recorded per each sample independently.



1201  
1202  
1203  
1204

**Extended Data Figure 1. Representative gating strategy for Hi-D FACS data.**

Representative gating of blood (a) and ETA (b) samples. Extracellular stain FMOs for markers used to interrogate neutrophil phenotype in blood (c) and ETA (d).

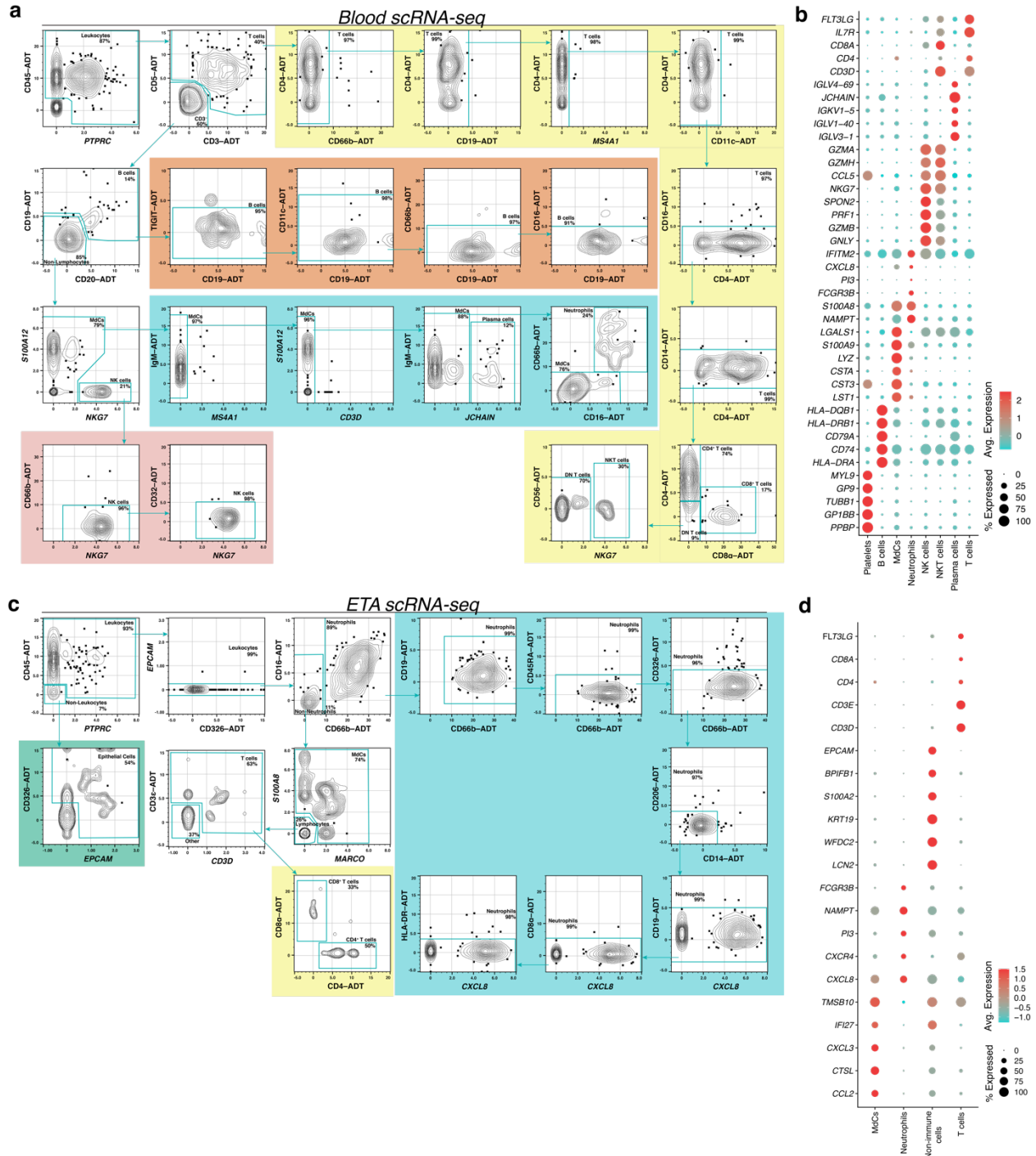


1205  
1206  
1207  
1208  
1209  
1210  
1211

**Extended Data Figure 2. Additional cytokine assessment in blood and lungs.**

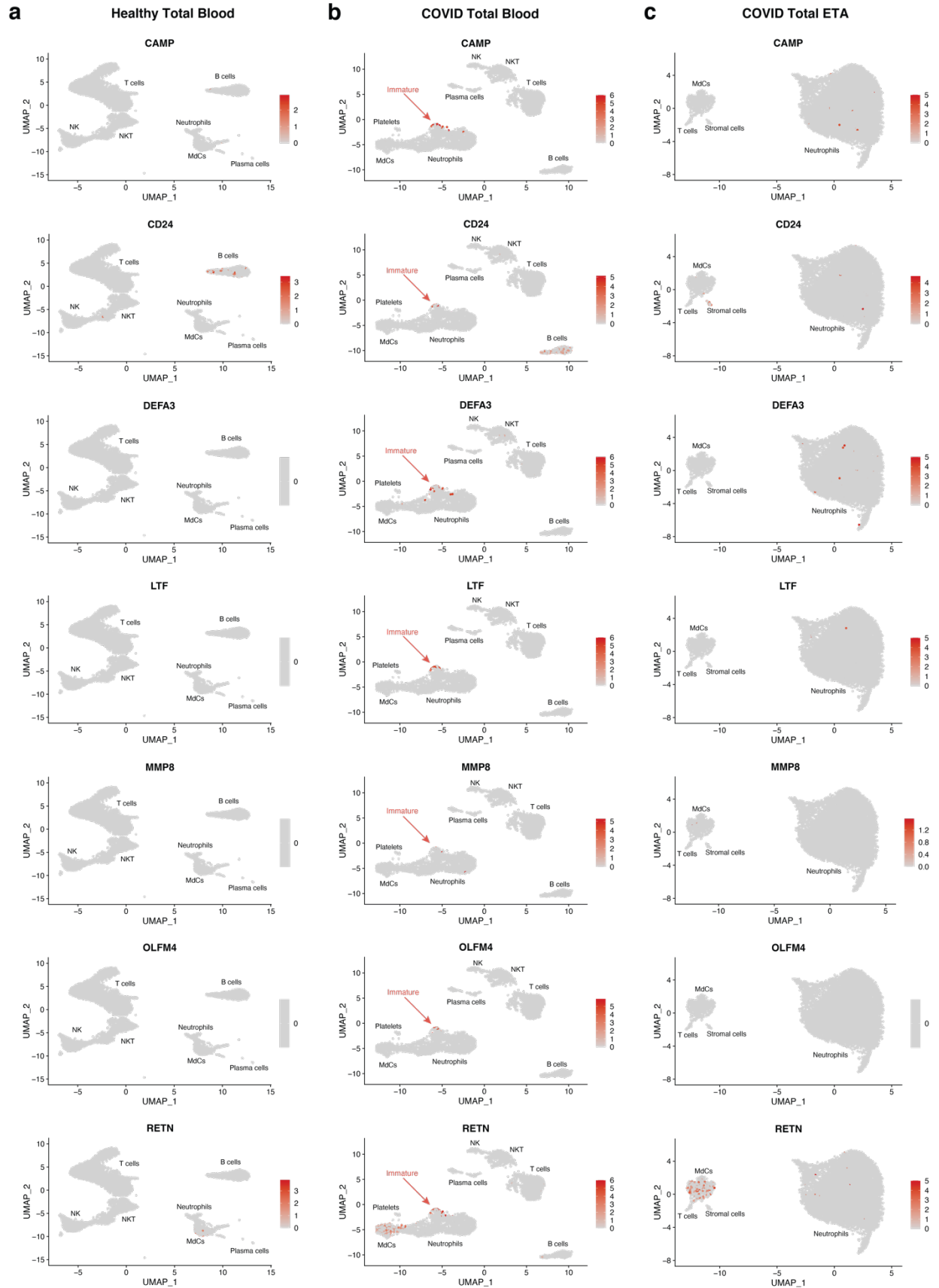
Concentration (pg/mL) of remaining 6 analytes interrogated by Mesoscale analyses in plasma (gray circles) and respiratory supernatant (Resp. SNT; green squares) from healthy control (HC), mild-acute (MA), and severe COVID-19 patients. Dotted line = assay limit of detection (LOD).



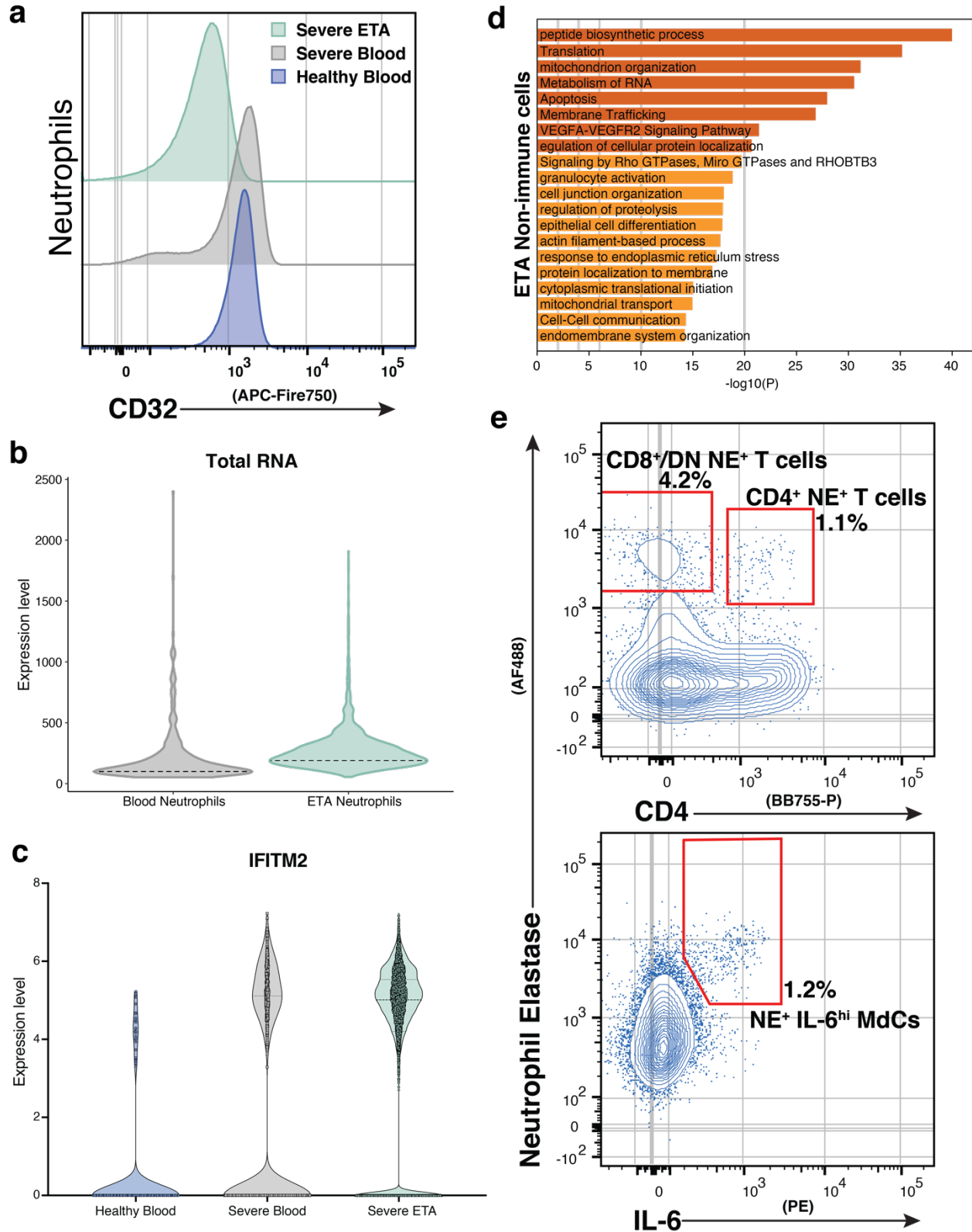


1212  
1213  
1214  
1215  
1216  
1217  
1218  
1219  
1220

**Extended Data Figure 3. Multi-omic scRNA-seq analysis of leukocytes in the blood and lung.** Gating strategy (a and c) employed to classify major lineages of immune cells by surface antibody-derived tag (ADT) and dot plots of the intersection of the top differentially expressed genes sorted by average log-fold change across cell populations (b and d) from the blood (a-b) and ETA (c-d) of severe COVID-19 patients using the SuPPER-seq pipeline previously described<sup>30</sup>.



1222 **Extended Data Figure 4. Gene signature for immature neutrophils is lacking in healthy**  
1223 **donors and lungs of COVID-19 patients.** UMAP visualizations of genes that identify immature  
1224 neutrophils in the blood healthy individuals (a) and severe COVID-19 patients (b), along with  
1225 cells from the lungs of severe COVID-19 patients (c).  
1226



1227  
1228

1229

1230

**Extended Data Figure 5. Cellular signatures during SARS-CoV-2 pathogenesis.** (a) Pulmonary neutrophils have a reduction in CD32 (FcγRII) expression as compared to circulating

1231 neutrophils. (b) Neutrophils undergo transcriptional reprogramming and increase de novo  
1232 transcription (total RNA) upon migrating to the lung. (c) Neutrophils in the blood and lung  
1233 increase expression of *IFITM2* during SARS-CoV-2 pathogenesis. (d) Metascape<sup>85</sup> pathway and  
1234 process enrichment analyses reveal non-immune cells have an increased gene signature for  
1235 granulocyte activation in the airways of severe COVID-19 patients. (e) Extracellular neutrophil  
1236 elastase is also detected on the surface of pulmonary T cells and myeloid-derived cells (MDCs)  
1237 in severe COVID-19 patients.  
1238  
1239  
1240